Search for physics beyond the standard model in top quark production with additional leptons in the context of effective field theory

The CMS collaboration

E-mail: cms-publication-committee-chair@cern.ch

ABSTRACT: A search for new physics in top quark production with additional final-state leptons is performed using data collected by the CMS experiment in proton-proton collisions at $\sqrt{s} = 13\,\text{TeV}$ at the LHC during 2016–2018. The data set corresponds to an integrated luminosity of $138\,\text{fb}^{-1}$. Using the framework of effective field theory (EFT), potential new physics effects are parametrized in terms of 26 dimension-six EFT operators. The impacts of EFT operators are incorporated through the event-level reweighting of Monte Carlo simulations, which allows for detector-level predictions. The events are divided into several categories based on lepton multiplicity, total lepton charge, jet multiplicity, and b-tagged jet multiplicity. Kinematic variables corresponding to the transverse momentum (p_T) of the leading pair of leptons and/or jets as well as the p_T of on-shell Z bosons are used to extract the 95% confidence intervals of the 26 Wilson coefficients corresponding to these EFT operators. No significant deviation with respect to the standard model prediction is found.

Contents

1 Introduction

Searches for new fundamental particles and interactions are motivated by the strong evidence for phenomena (such as dark matter [1, 2]) that are not described by the standard model (SM) of particle physics. However, there is no a priori reason to assume that particles will be light enough to be produced on-shell at the CERN LHC. Indirect methods of probing higher energy scales are thus an important part of searches for new physics at the energy frontier. One example of this type of approach is effective field theory (EFT), a

flexible framework that comprehensively describes the off-shell effects of new physics phenomena at a mass scale Λ. The EFT treats the SM Lagrangian as the lowest order term in an expansion of a more complete Lagrangian at a mass scale Λ in the form of a series of higher-dimensional operators, which are built from products of SM fields that respect the SM symmetries. The EFT Lagrangian is written as

$$\mathcal{L}_{\text{EFT}} = \mathcal{L}_{\text{SM}} + \sum_{d,i} \frac{c_i^d}{\Lambda^{d-4}} \mathcal{O}_i^d, \tag{1.1}$$

where $\mathcal{L}_{\text{SM}}$ is the SM Lagrangian, $\mathcal{O}_i^d$ are the EFT operators of dimension d, and c_i^d are the Wilson coefficients (WCs) which control the strength of the EFT effects. Since each higher order term in eq. (1.1) is suppressed by powers of Λ^{d-4}, the smallest dimension operators tend to produce the largest expected deviations from the SM ($d \leq 4$) processes. We do not consider operators that violate baryon or lepton number, so all operators of odd dimension are excluded, making the dimension-six operators the leading new physics contributions [3]. The next contributions would arise from dimension-eight operators, which are not considered here.

This paper focuses specifically on operators that couple the top quark to leptons, bosons, and other heavy (top or bottom) quarks. Searching for new physics in the top quark sector is motivated by the uniquely large mass of the top quark [4, 5] and the resulting Yukawa coupling to the Higgs field [6] of roughly unity. The LHC provides a rich environment of top quarks produced with additional leptons. Furthermore, the leptonic final-state decays of the top quark provide experimentally clean signatures with relatively low background contributions. The dominant SM contributions to these signatures arise from processes in which one or more top quarks are produced in association with a heavy boson or other top quarks. Referred to as associated top quark production, these processes include $t\bar{t}H$ [7], $t\bar{t}W$ [8], $t\bar{t}Z$ [9], tZq [10], tHq [7], $t\bar{t}t\bar{t}$ [11]. While each of these processes have been studied individually, the analysis presented in this paper takes a more global approach, using the EFT framework to probe the potential effects of heavy new physics impacting these associated top quark processes simultaneously. In addition to these SM contributions, the analysis also aims to probe new physics effects that may impact these final state signatures without an intermediate boson (via a four-fermion EFT vertex).

The analysis described in this paper builds on the approach developed in ref. [12], which studied 16 dimension-six EFT operators with data collected in 2017, corresponding to an integrated luminosity of $41.5\,\text{fb}^{-1}$. With this approach, EFT effects are incorporated into the event weights of the simulated samples, allowing detector-level predictions that account for all relevant interference effects (not only between new physics and the SM, but also among new physics operators) and correlations among WCs. This approach has been subsequently utilized to study $t\bar{t}Z$, tZq, and tWZ [13] and to study $t\bar{t}H$ and $t\bar{t}Z$ processes in which the Higgs or Z boson is boosted [14]; the former simultaneously probes five WCs, while the latter simultaneously probes eight WCs. Expanding on these previous analyses, we study the effects of 26 operators, incorporate additional signatures, and improve the sensitivity by fitting differential kinematical distributions and making use of all

data collected by the CMS experiment in 2016–2018, corresponding to a total integrated luminosity of $138\,\text{fb}^{-1}$. This paper thus represents the most global detector-level EFT analysis to date.

The sections in this paper are organized as follows. The CMS detector is introduced in section 2. In section 3, the data and simulated samples are discussed. The object reconstruction and event selection are covered in sections 4 and 5. Section 6 describes the background estimation. The statistical methods are explained in section 7, and the systematic uncertainties are detailed in section 8. Section 9 presents the results, which are summarized in section 10. The tabulated results are provided in the HEPData record for this analysis [15].

2 The CMS detector

The central feature of the CMS apparatus is a superconducting solenoid of 6 m internal diameter, providing a magnetic field of 3.8 T. Within the solenoid volume are a silicon pixel and strip tracker, a lead tungstate crystal electromagnetic calorimeter (ECAL), and a brass and scintillator hadron calorimeter (HCAL), each composed of a barrel and two endcap sections. Forward calorimeters extend the pseudorapidity (η) coverage provided by the barrel and endcap detectors. Muons are measured in gas-ionization detectors embedded in the steel flux-return yoke outside the solenoid. A more detailed description of the CMS detector, together with a definition of the coordinate system used and the relevant kinematic variables, can be found in ref. [16].

Events of interest are selected using a two-tiered trigger system. The first level (L1), composed of custom hardware processors, uses information from the calorimeters and muon detectors to select events at a rate of around 100 kHz within a fixed latency of about $4\,\mu\text{s}$ [17]. The second level, known as the high-level trigger, consists of a farm of processors running a version of the full event reconstruction software optimized for fast processing, and reduces the event rate to around 1 kHz before data storage [18].

3 Data samples and signal simulation

This analysis uses data from proton-proton collisions at $\sqrt{s} = 13\,\text{TeV}$ collected by the CMS experiment during 2016–2018 with a combination of single-, double-, and triple-lepton triggers. The minimum lepton transverse momentum (p_T) requirements are chosen such that all events are within the fully efficient regions of the triggers. The trigger efficiencies, calculated using independent missing transverse energy triggers, are higher than 95% across the full p_T spectrum with uncertainties, systematic and statistical, smaller than 2%.

The analysis aims to study dimension-six EFT effects on processes in which top quarks are produced in association with additional charged leptons. Processes that lead to the same multilepton final-state signatures but are not impacted by these EFT operators are backgrounds for this analysis. The expected background contributions are estimated using a combination of simulated samples and control samples in data, as described in section 6.
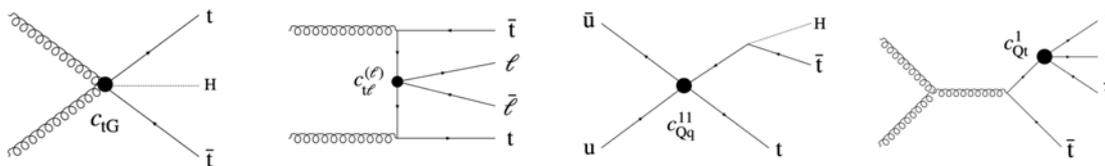
Figure 1. Example Feynman diagrams illustrating Wilson coefficients from each of the categories listed in table 1. From left to right, the diagrams show vertices associated with the c_{tG}, $c_{t\ell}^{(\ell)}$, c_{Qq}^{11}, and c_{Qt}^1.

The signal contribution is modeled at leading order (LO) using the MAD-GRAPH5_aMC@NLO event generator (version 2.6.5) [19–21] with the DIM6TOP model described in ref. [22] to incorporate the EFT effects. Using the Warsaw basis [23] of gauge invariant dimension-six operators, this model focuses on operators involving one or more top quarks, providing tree-level modeling of their effects. While the model described in ref. [22] allows for the EFT effects to vary independently for each generation of leptons, we impose the assumption that the EFT effects impact each lepton generation in the same way. In this analysis, we aim to include all operators from ref. [22] that significantly impact processes in which one or more top quarks are produced in association with charged leptons; as listed in table 1, this amounts to 26 operators in total. The 26 operators fall into four main categories: operators involving four heavy quarks (4hq), operators involving two heavy quarks and two light quarks (2hq2lq), operators involving two heavy quarks and two leptons (2hq2ℓ), and operators involving two heavy quarks and bosons (2hqV). The leptons in the 2hq2ℓ operators may be either charged or neutral, and the bosons in the 2hqV operators include both gauge bosons and the Higgs boson. Figure 1 shows examples of how WCs from each of these categories can impact associated top processes. The definitions of the operators associated with all of these WCs are provided in ref. [22]. In order to allow MADGRAPH5_aMC@NLO to properly handle the emission of gluons from the vertices involving the c_{tG} WC (which impacts interactions involving top quarks, gluons, and the Higgs boson), an extra factor of the strong coupling g_s is applied to the c_{tG} coefficient, as explained in ref. [24]. The simulations use the NNPDF3.1 [25] sets of parton distribution functions (PDFs). Parton showering and hadronization are performed with PYTHIA 8.240 [26] with the CP5 tune [27]. The decays of Higgs bosons and top quarks are handled with PYTHIA. Both the leptonic and hadronic top quark decays can contribute. The top quark mass used in the simulation is 172.5 GeV. The default input scheme in the DIM6TOP model is used. The $t\ell\bar{\ell}q$ and tHq samples are produced using the four-flavor scheme, while the five-flavor scheme is used for the rest of the samples ($t\bar{t}H$, $t\bar{t}\ell\bar{\ell}$, $t\bar{t}\ell\nu$, and $t\bar{t}t\bar{t}$).

Processes that are significantly impacted by these operators constitute the signal processes for this analysis: $t\bar{t}H$, $t\bar{t}\ell\bar{\ell}$, $t\bar{t}\ell\nu$, $t\ell\bar{\ell}q$, tHq, and $t\bar{t}t\bar{t}$. The $t\bar{t}\ell\bar{\ell}$ and $t\ell\bar{\ell}q$ samples incorporate contributions from on- and off-shell Z bosons, contributions from virtual photons, and contributions in which the lepton pair is produced directly from a 2hq2ℓ EFT

Operator category	Wilson coefficients
Two-heavy (2hqV)	$c_{t\varphi}$, $c_{\varphi Q}^{-}$, $c_{\varphi Q}^{3}$, $c_{\varphi t}$, $c_{\varphi tb}$, c_{tW}, c_{tZ}, c_{bW}, c_{tG}
Two-heavy-two-lepton (2hq2ℓ)	$c_{Q\ell}^{3(\ell)}$, $c_{Q\ell}^{-(\ell)}$, $c_{Qe}^{(\ell)}$, $c_{t\ell}^{(\ell)}$, $c_{te}^{(\ell)}$, $c_{t}^{S(\ell)}$, $c_{t}^{T(\ell)}$
Two-heavy-two-light (2hq2lq)	c_{Qq}^{31}, c_{Qq}^{38}, c_{Qq}^{11}, c_{Qq}^{18}, c_{tq}^{1}, c_{tq}^{8}
Four-heavy (4hq)	c_{QQ}^{1}, c_{Qt}^{1}, c_{Qt}^{8}, c_{tt}^{1}

Table 1. List of Wilson coefficients (WCs) included in this analysis, grouped according to the categories of WCs defined in ref. [22]; the abbreviations for the WCs categories used in this paper are noted parenthetically. The definitions of the WCs and the definitions of the corresponding operators can be found in table 1 of ref. [22]. An extra factor of the strong coupling is applied to the c_{tG} coefficient, as explained in the text.

Process	Cross section (pb)	Accuracy	Ref.
$t\bar{t}H$	$0.5071 \pm 2.4\%\,(\text{PDF})\,^{+7.6\%}_{-7.1\%}\,(\text{QCD})$	NLO (QCD + EWK)	[28]
$t\bar{t}\ell\bar{\ell}$ ($m_{\ell\ell} > 10\,\text{GeV}$)	$0.113^{+12\%}_{-10\%}\,(\text{QCD})$	NLO (QCD + EWK)	[28]
$t\bar{t}\ell\nu$	$0.235^{+10\%}_{-11\%}\,(\text{QCD})$	NLO (QCD + EWK) (incl. $\alpha_S\alpha^4$ terms and multijet merging)	[29]
$t\ell\bar{\ell}q$ ($m_{\ell\ell} > 30\,\text{GeV}$)	$0.076 \pm 2.7\%\,(\text{PDF}) \pm 2.0\%\,(\text{QCD})$	NLO QCD	[19–21]
tHq	$0.071 \pm 5.1\%\,(\text{PDF})\,^{+6.5\%}_{-15\%}\,(\text{QCD})$	NLO QCD	[28]
$t\bar{t}t\bar{t}$	$0.01337 \pm 6.9\%\,(\text{PDF})\,^{+3.6\%}_{-11\%}\,(\text{QCD})$	NLO (QCD + EWK) + NLL'	[30]

Table 2. Theoretical cross sections at next-to-LO (NLO) used for normalization of simulated signal samples. The items are ordered by cross section. The uncertainties are broken into normalization components due to modeling the parton distribution functions (PDFs) and QCD order. Entries without a value are negligible.

vertex. The $t\bar{t}\ell\nu$ process similarly includes lepton pairs produced from on-shell W bosons, as well as those from nonresonant processes, allowing the effects from 2hq2ℓ operators to be incorporated in the sample. The processes involving a Higgs boson enter our signal selection (defined in section 5) when the Higgs boson decays into one or more leptons. All simulated signal processes are normalized with their respective cross sections which are given table 2. The cross section computations may include quantum chromodynamics (QCD) and electroweak (EWK) corrections.

For each of the six signal processes, we account for diagrams with zero EFT vertices (i.e., the SM contribution) and diagrams with one EFT vertex (i.e., the new physics contribution). The amplitude for each process will thus depend linearly on the WCs, and the cross section will depend quadratically on the WCs. With 26 WCs, the dependence of the cross section on the WCs will therefore be given by a 26-dimensional quadratic function. Since the weight of each generated event corresponds to the event's contribution to the inclusive cross section, each event weight will also depend quadratically on the 26 WCs. For

each generated event, we determine the 26-dimensional quadratic parametrization using the MADGRAPH5_aMC@NLO event reweighting technique [31]. Once we have obtained the 26-dimensional quadratic parametrization for each event, we can find the dependence of any observable bin (i.e., distinct category of events defined by the properties of the final-state objects) on the WCs by summing the quadratic parametrizations for each of the events that passes the selection criteria for the given bin. Since we are thus able to write the predicted yield of any observable bin as a function of the 26 WCs, we can obtain detector-level predictions at any arbitrary point in the 26-dimensional EFT space. This is the key enabling concept of this analysis, and it allows us to rigorously account for all EFT effects across all analysis bins simultaneously when performing the likelihood fitting with the statistical framework. This approach was developed in ref. [12], which contains a more detailed description of the method of parametrizing the predicted yields in terms of the WCs.

Similar to ref. [12], we include an additional final-state parton in the matrix element generation for the $t\bar{t}X$ processes using the MLM scheme [21]. The inclusion of the additional parton can improve the modeling at high jet multiplicities, and can also significantly impact the dependence of the $t\bar{t}X$ processes on the WCs [24]. For the other processes ($t\ell\bar{\ell}q$, tHq, and $t\bar{t}t\bar{t}$), an additional jet is not included because of technical limitations, and an additional uncertainty is applied to account for this where relevant, as described in section 8.

4 Object reconstruction and identification

The global event reconstruction (also called particle-flow event reconstruction [32]) aims to reconstruct and identify each individual particle in an event, with an optimized combination of all subdetector information. In this process, the identification of the particle type (photon (γ), electron, muon, charged hadron, neutral hadron) plays an important role in the determination of the particle direction and energy. Photons are identified as ECAL energy clusters not linked to the extrapolation of any charged particle trajectory to the ECAL. Electrons are identified as a primary charged particle track and potentially many ECAL energy clusters corresponding to this track extrapolation to the ECAL and to possible bremsstrahlung photons emitted along the way through the tracker material. Muons are identified as tracks in the central tracker consistent with either a track or several hits in the muon system, and associated with calorimeter deposits compatible with the muon hypothesis. Charged hadrons are identified as charged particle tracks neither identified as electrons, nor as muons. Finally, neutral hadrons are identified as HCAL energy clusters not linked to any charged hadron trajectory, or as a combined ECAL and HCAL energy excess with respect to the expected charged hadron energy deposit.

The energy of photons is obtained from the ECAL measurement. The energy of electrons is determined from a combination of the track momentum at the main interaction vertex, the corresponding ECAL cluster energy, and the energy sum of all bremsstrahlung photons attached to the track. The energy of muons is obtained from the corresponding track momentum. The energy of charged hadrons is determined from a combination of the track momentum and the corresponding ECAL and HCAL energies, corrected for the

response function of the calorimeters to hadronic showers. Finally, the energy of neutral hadrons is obtained from the corresponding corrected ECAL and HCAL energies.

The electron momentum is estimated by combining the energy measurement in the ECAL with the momentum measurement in the tracker. The momentum resolution for electrons with $p_T \approx 45\,\text{GeV}$ from $Z \to ee$ decays ranges from 1.6 to 5%. It is generally better in the barrel region than in the endcaps, and also depends on the bremsstrahlung energy emitted by the electron as it traverses the material in front of the ECAL [33, 34]. We require electrons to have pseudorapidity $|\eta| < 2.5$.

Muons are measured in the pseudorapidity range $|\eta| < 2.4$, with detection planes made using three technologies: drift tubes, cathode strip chambers, and resistive plate chambers. The single muon trigger efficiency exceeds 90% over the full η range, and the efficiency to reconstruct and identify muons is greater than 96%. Matching muons to tracks measured in the silicon tracker results in a relative transverse momentum resolution, for muons with p_T up to 100 GeV, of 1% in the barrel and 3% in the endcaps. The p_T resolution in the barrel is better than 7% for muons with p_T up to 1 TeV [35].

Reconstructed electrons and muons are required to satisfy selection criteria aiming to select prompt leptons produced in decays of the W or Z bosons, as well as those that couple directly to the top quarks in the beyond-SM scenarios we consider. This lepton selection, fully described in ref. [7], is performed by means of a multivariate discriminator [36] that takes as its input the variables related to the lepton isolation and its impact parameter. In addition, kinematic information of charged and neutral particles around the lepton candidate is used by feeding it into the jet reconstruction and b tagging algorithms, described below. The score of the b tagging algorithm is used as an input to the discriminator.

The hadronic jets are clustered using the infrared and collinear safe anti-k_T algorithm [37, 38] with a distance parameter of 0.4. Jet momentum is determined as the vectorial sum of all particle momenta in the jet, and is found from simulation to be, on average, within 5 to 10% of the true momentum over the whole p_T spectrum and detector acceptance. Additional proton-proton interactions within the same or nearby bunch crossings (pileup) can contribute additional tracks and calorimetric energy depositions to the jet momentum. To mitigate this effect, charged particles identified to be originating from pileup vertices are discarded and an offset correction is applied to correct for remaining contributions [39]. Jet energy corrections are derived from simulation to bring the measured response of jets to that of particle level jets on average. In situ measurements of the momentum balance in dijet, γ + jet, Z + jet, and multijet events are used to account for any residual differences in the jet energy scale (JES) between data and simulation [40]. The jet energy resolution (JER) amounts typically to 15–20% at 30 GeV, 10% at 100 GeV, and 5% at 1 TeV [40]. Additional selection criteria are applied to each jet to remove jets potentially dominated by anomalous contributions from various subdetector components or reconstruction failures.

Jets originating from b quark decays (b jets) are identified using the algorithm [41] known as DEEPJET [42, 43], which uses a deep neural network to classify b jets with different working points. The analysis uses a medium working point which correctly identifies b jets with an efficiency of about 70%, and a loose working point with an efficiency of about 85%. The misidentification rate for gluon or light-flavor quark jets for these two working points is 1.0% and 10%, respectively.
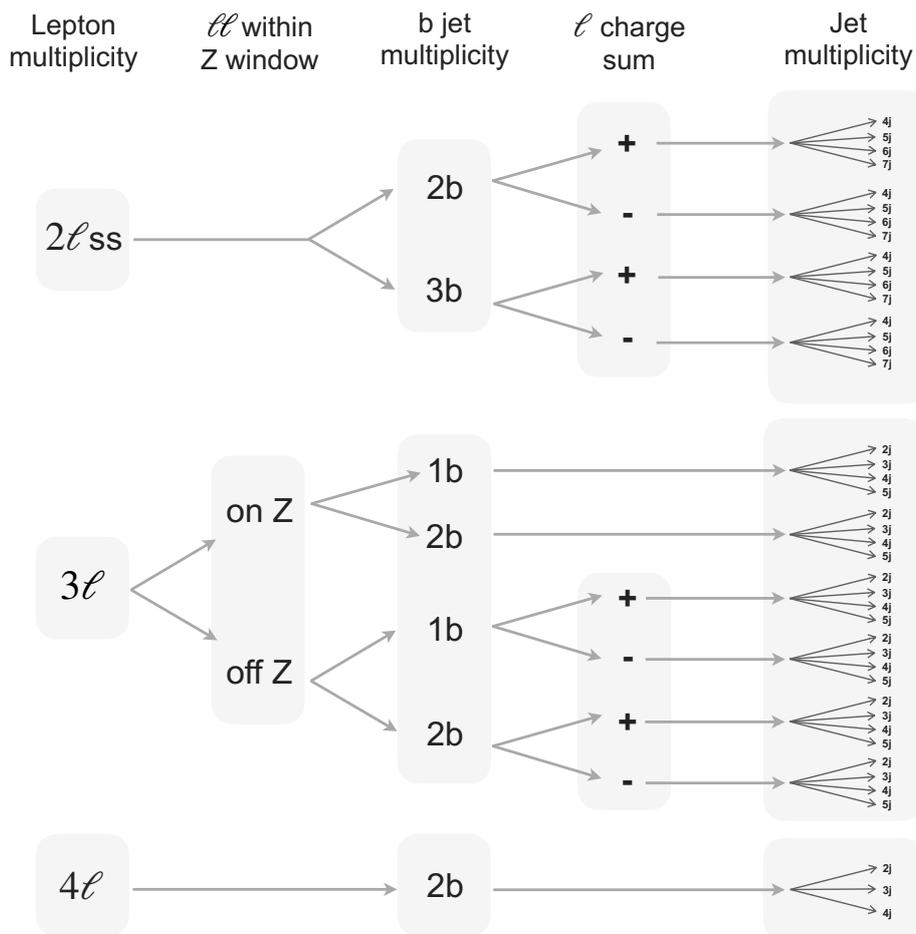
Figure 2. Summary of the event selection categorization. The details for the selection requirements are described in sections 5.1–5.3.

5 Event selection and categorization

The analysis targets events in which top quarks are produced in association with additional charged leptons. The event selection categories are defined primarily by the multiplicity of charged leptons, jets, and b jets. This event selection scheme aims to isolate subsamples of the broader multilepton data set into categories containing different admixtures of the contributing signal processes, resulting in 43 unique categories. The events in each category are binned according to a kinematical variable, which will be described in section 5.4. While it is not possible to completely isolate any of these individual processes, the division of the sample into subsamples with different compositions increases the statistical power to determine which specific processes might be responsible for any deviation from SM expectations that may be observed in data.

We require each event to have either two same-sign leptons (2ℓss), three leptons (3ℓ), or four or more leptons (4ℓ). The 3ℓ event category is further subdivided into events with and without on-shell Z boson decays (pair of same-flavor and opposite-sign leptons with an invariant mass within 10 GeV of the Z boson mass), referred to as the on-Z and off-Z

Event category	Leptons	$m_{\ell\ell}$	b tags	Lepton charge sum	Jets	Kinematical variable
2ℓss 2b	2	No requirement	2	>0, <0	4, 5, 6, $\geq$7	$p_{\mathrm{T}}(\ell\mathrm{j})_{\max}$
2ℓss 3b	2	No requirement	$\geq$3	>0, <0	4, 5, 6, $\geq$7	$p_{\mathrm{T}}(\ell\mathrm{j})_{\max}$
3ℓ off-Z 1b	3	$|m_{\mathrm{Z}} - m_{\ell\ell}| > 10\,\mathrm{GeV}$	1	>0, <0	2, 3, 4, $\geq$5	$p_{\mathrm{T}}(\ell\mathrm{j})_{\max}$
3ℓ off-Z 2b	3	$|m_{\mathrm{Z}} - m_{\ell\ell}| > 10\,\mathrm{GeV}$	$\geq$2	>0, <0	2, 3, 4, $\geq$5	$p_{\mathrm{T}}(\ell\mathrm{j})_{\max}$
3ℓ on-Z 1b	3	$|m_{\mathrm{Z}} - m_{\ell\ell}| < 10\,\mathrm{GeV}$	1	No requirement	2, 3, 4, $\geq$5	$p_{\mathrm{T}}(\mathrm{Z})$
3ℓ on-Z 2b	3	$|m_{\mathrm{Z}} - m_{\ell\ell}| < 10\,\mathrm{GeV}$	$\geq$2	No requirement	2, 3, 4, $\geq$5	$p_{\mathrm{T}}(\mathrm{Z})$ or $p_{\mathrm{T}}(\ell\mathrm{j})_{\max}$
4ℓ	$\geq$4	No requirement	$\geq$2	No requirement	2, 3, $\geq$4	$p_{\mathrm{T}}(\ell\mathrm{j})_{\max}$

Table 3. Object requirements for the 43 event selection categories. Requirements separated by commas indicate a division into subcategories. The kinematical variable that is used in the event category is also listed. Section 5.4 provides further details regarding the kinematical distributions.

subcategories, respectively. The events in the 3ℓ off-Z category and in the 2ℓss category are subdivided based on the sum of the charges of the leptons. A schematic summary of the event selection categorization is shown in figure 2. The selected events in all categories must have at least two jets with $p_{\mathrm{T}} > 30\,\mathrm{GeV}$ and $|\eta| < 2.4$. Events containing a pair of leptons with an invariant mass of less than 12 GeV are rejected to avoid backgrounds from light resonances. We use the DEEPJET algorithm to impose the further requirement of one or more b-tagged jets, depending on the lepton multiplicity. The τ leptons only enter our event selections via their $\tau \to \mathrm{e}$ and $\tau \to \mu$ decay modes. Table 3 provides a summary of the requirements for each event category, which are detailed in the following sections.

5.1 The 2ℓss event category

The 2ℓss event category targets $\mathrm{t\bar{t}H}$, $\mathrm{t\bar{t}}\ell\nu$, and $\mathrm{t\bar{t}t\bar{t}}$ events, where the events contain two leptons of the same charge which must pass the tight object selection criteria. The higher (lower) p_{T} lepton must have $p_{\mathrm{T}} > 25\,(15)\,\mathrm{GeV}$. The charge requirement significantly reduces $\mathrm{t\bar{t}}$ + jets background by leveraging the precision of the CMS detector to reliably reconstruct the electron and muon charges. We require the uncertainty in the muon p_{T} to be smaller than 20% and apply electron selection criteria, described as the "selective algorithm" in ref. [33], that demand the consistency among three independent measurements of the electron charge, based on two different parametrizations of the electron track and the relative positions of the electron track and its energy deposit in the ECAL. The 2ℓss events must have jet multiplicity of $\geq$4 with $p_{\mathrm{T}} > 30\,\mathrm{GeV}$ and $|\eta| < 2.4$. We also split the 2ℓss events based on total lepton charge because the $\mathrm{t\bar{t}W^{+}}$ cross section in proton-proton collisions is roughly twice that of the $\mathrm{t\bar{t}W^{-}}$ cross section. The 2ℓss events are further subdivided based on b jet multiplicity, which helps target $\mathrm{t\bar{t}t\bar{t}}$ events since events with higher numbers of b-tagged jets are enriched in $\mathrm{t\bar{t}t\bar{t}}$ events.

5.2 The 3ℓ event category

The 3ℓ event category targets $\mathrm{t\bar{t}}\ell\bar{\ell}$, $\mathrm{t}\ell\bar{\ell}\mathrm{q}$, $\mathrm{t\bar{t}H}$, and $\mathrm{t\bar{t}}\ell\nu$ events. This category requires exactly three leptons to pass the tight selection criteria. The first, second, and third leptons must be above the p_{T} threshold of 25, 15, and 10 GeV, respectively. In case the third lepton is an electron, the threshold is $p_{\mathrm{T}} > 15\,\mathrm{GeV}$, which suppresses the contributions

from nonprompt electrons and helps stay above trigger thresholds. We also require at least two jets with $p_T > 30\,\mathrm{GeV}$. In the 3ℓ event category, we separate events which contain a same-flavor opposite-sign pair of leptons with a mass within $10\,\mathrm{GeV}$ of m_Z ($91.2\,\mathrm{GeV}$) in order to isolate an enhanced contribution from the on-shell Z boson decay, primarily from the $\mathrm{t\bar{t}Z}$ process. Events that do not lie within this region are further separated based on whether the sum of the lepton charges is positive or negative to again exploit the difference in cross section between $\mathrm{t\bar{t}W^+}$ and $\mathrm{t\bar{t}W^-}$. All 3ℓ events are also categorized by the number of b jets passing the medium DEEPJET working point: exactly one b jet, or ≥ 2 b jets. Requiring one b jet enhances $\mathrm{t\ell\bar{\ell}q}$ events, while requiring ≥ 2 b jets helps to separate $\mathrm{t\ell\bar{\ell}q}$ and $\mathrm{t\bar{t}\ell\bar{\ell}}$ events.

5.3 The 4ℓ event category

The 4ℓ event category targets $\mathrm{t\bar{t}\ell\bar{\ell}}$ and $\mathrm{t\bar{t}H}$ events, requiring at least four leptons passing the specific selection criteria. The first through fourth leptons must be above the p_T threshold of 25, 15, 10, and $10\,\mathrm{GeV}$, respectively. If the last two leptons are electrons, the requirement becomes $p_T > 15\,\mathrm{GeV}$ for both because of the same reasons described in the 3ℓ event category. The events must have at least two jets with $p_T > 30\,\mathrm{GeV}$ and $|\eta| < 2.4$. At least two of these jets must be b jets, where one of them is required to pass the DEEPJET medium working point, while the second is allowed to pass the loose working point.

5.4 Kinematical variables

The selections described in sections 5.1–5.3 result in 43 unique categories of events. In order to gain additional sensitivity to EFT effects, the events in each of the 43 categories are binned according to a kinematical variable.

For most of the event categories, we use the variable $p_T(\ell\mathrm{j})_{\mathrm{max}}$. To form this variable, we sum vectorially the momenta of all possible pairs of objects in the collections of leptons and jets and select the combination with the largest p_T. The value of $p_T(\ell\mathrm{j})_{\mathrm{max}}$ is the p_T of that combination. Thus, this variable may represent the transverse momenta of two leptons, two jets, or a lepton and a jet. Expressed mathematically, the $p_T(\ell\mathrm{j})_{\mathrm{max}}$ variable can be described as follows:

$$p_T(\ell\mathrm{j})_{\mathrm{max}} = \max\left(\max\left[p_T(\ell, \ell')\right], \max\left[p_T(\mathrm{j}, \mathrm{j}')\right], \max\left[p_T(\ell, \mathrm{j})\right]\right), \qquad (5.1)$$

where $\max[p_T(\ell, \ell')]$ indicates the p_T of the pair of unique leptons with the largest p_T, $\max[p_T(\mathrm{j}, \mathrm{j}')]$ indicates the p_T of the pair of unique jets with the largest p_T, and $\max[p_T(\ell, \mathrm{j})]$ indicates the p_T of the lepton-jet pair with the largest p_T. The $p_T(\ell\mathrm{j})_{\mathrm{max}}$ variable is useful because it combines sensitivity to a broad range of EFT effects that grow with energy with access to a combination of EFT operators involving jets and/or leptons. The $p_T(\ell\mathrm{j})_{\mathrm{max}}$ variable thus provides broadly good sensitivity to most of the WCs included in this analysis, motivating its use in the majority of the event categories. For most of the on-shell Z 3ℓ categories, however, we do not use $p_T(\ell\mathrm{j})_{\mathrm{max}}$. Instead, we use a variable that aims to provide sensitivity to the EFT operators involving Z bosons, as these operators may modify the kinematical variables of the Z boson. Denoted as $p_T(\mathrm{Z})$, this variable is
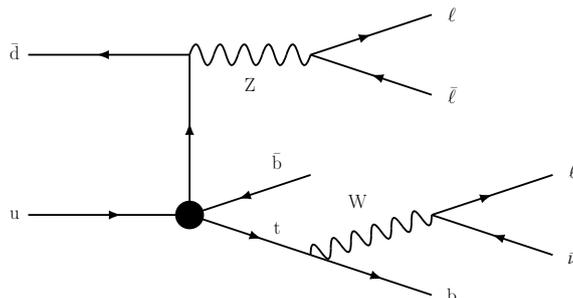
Figure 3. Example Feynman diagram illustrating how the c_{Qq}^{31} and c_{Qq}^{38} WCs can impact the processes in 3ℓ categories with two b quarks and an on-shell Z boson. These two WCs are a part of the 2hq2lq group, but unlike the other WCs in this group, these two WCs are associated with operators that have vertices involving a top and bottom quark pair, as pictured in the figure.

defined as the p_{T} of the same-flavor opposite-sign lepton pair associated with the Z boson. The $p_{\mathrm{T}}(\mathrm{Z})$ variable is used for all of the on-shell Z boson 3ℓ event categories, except for the event categories with two or three jets and two b jets. As shown in figure 3, events with c_{Qq}^{31} and c_{Qq}^{38} vertices can contribute to these final states, and in these cases the Z boson is not associated with the EFT vertex, so using $p_{\mathrm{T}}(\mathrm{Z})$ in these event categories decreases sensitivity to the c_{Qq}^{31} and c_{Qq}^{38} coefficients. For this reason, we utilize $p_{\mathrm{T}}(\ell\mathrm{j})_{\mathrm{max}}$ instead of $p_{\mathrm{T}}(\mathrm{Z})$ in these specific on-shell Z categories, since this more general variable provides good sensitivity to the c_{Qq}^{31} and c_{Qq}^{38} WCs.

In summary, the $p_{\mathrm{T}}(\mathrm{Z})$ variable is used for all of the on-shell Z categories, except for the two and three jet categories with two b-tagged jets; the $p_{\mathrm{T}}(\mathrm{Z})$ variable is thus used in a total of six event categories. In the remaining 37 event categories, the $p_{\mathrm{T}}(\ell\mathrm{j})_{\mathrm{max}}$ variable is used. For the categories that are binned in $p_{\mathrm{T}}(\ell\mathrm{j})_{\mathrm{max}}$, four bins are used. For the categories that are binned in $p_{\mathrm{T}}(\mathrm{Z})$ (which generally have larger numbers of selected events), five bins are used. This results in 178 total analysis bins. Binning the 43 analysis categories in terms of the $p_{\mathrm{T}}(\ell\mathrm{j})_{\mathrm{max}}$ and $p_{\mathrm{T}}(\mathrm{Z})$ variables provides an improvement in sensitivity of up to a factor of about two, compared to the case where the 43 analysis categories are not further subdivided.

6 Background estimation

In addition to contributions from signal processes, we expect contributions from other SM processes to the signal regions (SRs) defined above. We distinguish between reducible and irreducible backgrounds. A background is considered to be irreducible if all final state leptons are genuine prompt leptons. The contribution from irreducible backgrounds is dominated by diboson (WZ and ZZ) production, but we expect a subleading contribution from triboson and tWZ production processes. Although the tWZ process in principle could be impacted by a subset of the WCs studied in this analysis, the analysis does not have strong sensitivity to the effects (and the predicted contribution is also small, making up only about 3% of the total predicted yield); the process is therefore categorized as background. We estimate the contribution of these processes using simulations with the MadGraph5_aMC@NLO, powheg [44–48], and mcfm [49] programs. The WZ production

is normalized to the next-to-NLO in perturbative QCD and NLO in EWK theory [50]. For ZZ production, the $q\overline{q} \to ZZ$ samples are next-to-LO (NLO) in QCD and LO in electroweak [44, 45]; the $gg \to ZZ$ samples are LO, and their cross sections are scaled to match a cross section that is NLO in QCD [51]. The diboson contributions are modeled with POWHEG, MADGRAPH5_aMC@NLO and MCFM. The triboson and tWZ contributions are modeled with MADGRAPH5_aMC@NLO.

We distinguish three types of reducible backgrounds. The leading contribution is due to processes with nonprompt leptons (e.g., from the decay of b hadrons) in the final state. We estimate the contribution from these events following the misidentification probability (MP) method described in ref. [7]. This method is performed by selecting events passing all the criteria described in section 5 with the exception of those on leptons, which are required to pass a looser identification criteria, but to fail the full set of requirements described in section 4. This region, denoted as the application region, is enriched in events with nonprompt leptons, but resembling the kinematics of the events in the SR.

We obtain an estimation of the nonprompt-lepton contribution to the SR by weighting each event in the application region by a weight w, defined as

$$w = (-1)^{n+1} \prod_{i=1}^{n} \frac{f(p_{\mathrm{T}}, \eta)_i}{1 - f(p_{\mathrm{T}}, \eta)_i}, \tag{6.1}$$

where n is the number of leptons in the event failing the lepton selection criteria and $f(p_{\mathrm{T}}, \eta)_i$ is the MP, defined as the probability for a nonprompt lepton passing the looser lepton selection to pass the required selection. This probability is measured in a sample of multijet events collected by a set of low-p_{T} lepton triggers and is measured as a function of the lepton p_{T} and η, separately for electrons and muons. The validity of the method has been checked using samples of simulated $t\overline{t}$ and multijet events, as well as dedicated control regions (CRs), as well as dedicated 2ℓss control regions (CRs), which are defined with lower jet multiplicities than the 2ℓss SRs in order to ensure orthogonality with the SR.

An additional contribution to reducible backgrounds in the 2ℓss SR is due to cases in which the charge of one of the final state leptons is measured incorrectly. This contribution is dominated by $t\overline{t}$ events and is estimated by selecting events passing the same selection as the 2ℓss SR, but inverting the same-sign requirement on the dilepton system. Events in this region are weighted by the probability of each of the leptons to have their charge measured with the wrong sign. This probability is negligible for muons; however the probability for electrons is larger and we estimate it using simulations. Additionally, we compare the prediction from the simulation with the observation of a region enriched in $Z \to ee$, where the charge of one of the electrons has been measured with the incorrect sign. The two agree within the applied uncertainties (30%), but we correct for the residual differences by a constant scale factor (SF) in our prediction.

Finally, a small contribution arises from the conversion of photons interacting with the detector material. This contribution is significantly suppressed by the electron reconstruction and identification algorithms, since we require electron tracks to have hits in the innermost layers of the silicon tracker and we veto electron candidates that are matched

to a reconstructed photon conversion vertex. We estimate this contribution using $t\bar{t}\gamma$ simulation (similar to ref. [52]) at LO with MADGRAPH5_AMC@NLO.

7 Statistical methods

A maximum likelihood fit is performed across all of the analysis bins, treating the number of observed events in each bin as an independent Poisson measurement [53]. The total yield in each bin is parametrized as a quadratic function of the 26 WCs, which are the parameters of interest in the likelihood fit. The yield in each bin also depends on the effects of the systematic uncertainties (as listed in section 8), which are treated as nuisance parameters (NPs) in the likelihood fit. The likelihood has the functional form

$$L = \prod_{i=1}^{N_{\text{bins}}} P(n_i|\nu_i(c,\theta)) \prod_{j=1}^{N_{\text{NP}}} p(\hat{\theta}_j|\theta_j), \tag{7.1}$$

where $P(n_i|\nu_i(c,\theta))$ is the probability of observing n_i events in the i-th category given by the Poisson distribution, and $p(\hat{\theta}_j|\theta_j)$ is the prior probability for the j-th NP evaluated at the maximum likelihood estimate $\hat{\theta}_j$. As described in section 3, the number of expected events is parametrized as a quadratic function of the WCs. This can be expressed as

$$\nu_i(c,\theta) = \text{SM}_i(\theta) + \sum_j \frac{c_j}{\Lambda^2} l_{ij}(\theta) + \sum_j \frac{c_j^2}{\Lambda^4} q_{ij}(\theta) + \sum_{j \neq k} \frac{c_j c_k}{\Lambda^4} m_{ijk}(\theta), \tag{7.2}$$

where c are the WCs, θ are the NPs, and l_j, q_j, and m_{jk} respectively are the linear, quadratic, and cross-term structure constants of the parametrization. In order to find the 1 and 2 standard deviation (σ) confidence intervals (CIs) for each WC, a scan is performed over each WC, profiling the other 25 WCs and the NPs. The test statistic is then given by

$$\Lambda_p(c_i) = -2 \ln \frac{L(\hat{c}_i, \hat{\theta})}{L(c_i, \hat{\hat{\theta}})}, \tag{7.3}$$

where $\hat{c}_i$ and $\hat{\theta}$ are the values which maximize the likelihood, and $\hat{\hat{\theta}}$ corresponds to all the profiled parameters which maximize the likelihood at a particular WC value. The test statistic asymptotically follows a χ^2 distribution where the degrees of freedom correspond to the number of free parameters. The scan is performed over a discrete set of values for the selected WC; at each WC value, the likelihood fit finds the corresponding values of the other WCs and NPs which minimize the negative log-likelihood (NLL) function. The 1 and 2σ CIs are extracted at the points where the values of the test statistic curve are equal to the values of 1 and 4 respectively. In order to explore the effects of each WC individually (without interference between WCs), a scan is also performed where the other 25 WCs are held to their SM values of zero (instead of profiled). The 1 and 2σ CIs for this scan are extracted in the same way as the profiled fit. Simultaneous scans are also performed for a selected subset of WC pairs (denoted as 2D). The 2D scans are performed similarly to the single WC scans; we step through a discrete set of points for the pair of scanned WCs, with the other 24 WCs either profiled or fixed to their SM values of zero. The 68.3, 95.5, and 99.7% 2D CIs are extracted where test statistic is equal to 2.30, 6.18, and 11.83, respectively.

8 Systematic uncertainties

The systematic uncertainties for this analysis are split into two main categories: uncertainties which only affect the rate of the signal and background processes, and ones which affect both the rate and shape of the measured distributions. Shape uncertainties which are specified as fully correlated across all distributions and data-taking years are expressed as a single NP per systematic term. The sources of systematic uncertainties considered are the following: the integrated luminosity, the JES and JER, b jet tagging SFs, the theoretical cross section, the renormalization (μ_R) and factorization (μ_F) scales, the parton shower, the additional radiation, the electron and muon identification and isolation, the trigger efficiency, the pileup, the L1 ECAL trigger efficiency corrections, the misidentified-lepton rate, the charge misreconstruction rate, and the mismodeling of the jet multiplicity in diboson events A breakdown of the systematic uncertainties and their average impact on the nominal predicted yields can be found in table 4.

Integrated luminosity: The uncertainty in the integrated luminosity is estimated to be 1.6% [54–56] for the 2016–2018 data set.

Jet energy scale and resolution: These systematic uncertainties are evaluated by shifting the scale and resolution applied to the reconstructed jets by $\pm 1\sigma$ in bins of p_T and η. The JES uncertainty is correlated across years, and is modeled with a total of five independent parameters. The JER uncertainty is uncorrelated across years, and is modeled with a total of four independent parameters. The impact of the JES and JER uncertainties is on average 1% of the nominal prediction across all analysis bins.

b jet tagging SFs: The uncertainties resulting from the b tagging efficiency and misidentification rate are assessed by varying, within their uncertainties, the b tagging data-to-simulation SFs. The SFs for the heavy-flavor (b and c quark) jets are varied together, and the SFs for the light-flavor (gluon and u, d, and s quark) jets are also together, independently from the heavy-flavor SFs. The uncertainties for both flavor components are split into a component that is correlated across all data-taking years and components that are uncorrelated across all data-taking years. The impact of the b jet tagging uncertainty is on average 1% of the nominal prediction across all analysis bins.

Theoretical cross section: The predicted yields for all signal and background categories are normalized to their theoretical cross section values, calculated at NLO precision or greater, with the exception of $t\bar{t}\gamma$, which is LO. The theoretical uncertainties on these calculations come from the PDF choice and the choice of the QCD scales (μ_R and μ_F). The average uncertainty across all analysis bins due to the scales is 1–4% of the total nominal predicted rate, while that from the PDFs is 1%.

Renormalization and factorization scales: Uncertainties in the matrix element generators due to the μ_R and μ_F scales are measured by shifting the μ_R and μ_F up (down) by a factor of 2 (0.5) independently, which allows the shape of the variations

to be incorporated coherently across bins. Since the inclusive cross sections for the simulated samples are normalized to NLO predictions and the uncertainty on this overall normalization is already accounted for with the theoretical cross section uncertainty discussed above, the μ_R and μ_F systematic uncertainties do not impact the inclusive cross section.[1] Rather, these systematic uncertainties affect the kinematic shapes and, correspondingly, the acceptance. The uncertainty due to the choice of μ_R and μ_F is about 3% of the nominal prediction across all analysis bins.

Parton shower: The uncertainty due to initial- and final-state radiation (ISR and FSR) in the parton-shower simulation is estimated by varying the scale of each up (down) by a factor of 2 (0.5) respectively. The uncertainty due to the FSR and ISR modeling is on average 1–2% of the nominal prediction across all analysis bins.

Additional radiation: Because of parton-matching limitations in the MAD-GRAPH5_aMC@NLO generator, additional partons cannot be included in the single t ($t\ell\bar{\ell}q$ and tHq) LO EFT samples. Instead, the $t\ell\bar{\ell}q$ LO sample is compared to the NLO tZq sample. In each jet bin, any discrepancy not covered by the systematic uncertainties is ascribed as an additional radiation uncertainty. Since this is an uncertainty due to issues in MADGRAPH5_aMC@NLO t-channel simulations, the same uncertainty is also applied to the tHq sample. The average change in yield due to the additional radiation is 7% of the total nominal predicted rate.

Electron and muon identification and isolation: The lepton SFs used to correct the efficiency on simulation to reproduce the efficiency in data are derived with a "tag-and-probe" method [33, 35, 57]. The lepton identification, isolation, and tracking efficiency SF uncertainties are estimated and propagated to the final fitting variable distributions. The total uncertainty of the resulting SFs is the quadratic sum of the statistical and systematic uncertainties, for electrons and muons separately. The uncertainty in the electron (muon) SF results in about 2 (1)% variation of the nominal prediction across all analysis bins.

Trigger efficiency: The impact due to the uncertainty in the trigger efficiency is estimated as well by varying the SFs within their uncertainties separately for each data-taking year and final state. This uncertainty is treated as uncorrelated between data-taking years. The uncertainty is on average $\leq 1\%$ of the nominal prediction across all analysis bins.

Pileup: Effects due to the uncertainty in the distribution of the number of pileup interactions are evaluated by varying the total inelastic proton-proton cross section used to calculate the number of pileup interactions in data by 4.6% from its nominal value, which corresponds to a 1σ variation [58]. The uncertainty in each analysis category is on average 1% of the nominal prediction across all analysis bins.

---

[1]Because the precision of the $t\bar{t}\gamma$ cross section is LO, the μ_R and μ_F uncertainties impact both the inclusive cross section and the kinematic shape for this sample.

L1 ECAL trigger efficiency: To model the ECAL L1 trigger efficiency in 2016–2017 [17], a weight with its uncertainty is applied to the simulation. The uncertainty in the predicted yields due to the L1 ECAL trigger efficiency is about 1% of the total nominal predicted rate.

Misidentified-lepton rate: The misidentification rates used to estimate the nonprompt-lepton background are affected by a statistical uncertainty associated with the number of events in the kinematic region used in the measurement as well as by uncertainties due to the different composition of this measurement region and the SR. Three sources of systematic uncertainty are considered. The first uncertainty stems from the statistical uncertainty associated with the multijet measurement region, while the second accounts for the uncertainty in the subtraction of the prompt-lepton contribution from the yield in this region. The effect of these two uncertainties is taken into account as variations of the MP map overall scale, as well as the dependences on p_T and η. In addition to the measurement in the MP, the residual differences between the MP estimation with multijet and $t\bar{t}$ simulated samples is taken as an additional source of systematic uncertainty. The uncertainty in the misidentified-lepton rate is on average of 30% of the total expected misidentified leptons, and an average of 3% of the nominal prediction across all analysis bins.

Charge misreconstruction rate: An uncertainty of 30% is assigned to the yield of the misreconstructed-charge background to account for the differences observed between the prediction and data in the charge misidentification CR, as noted in section 6. The uncertainty in each analysis category is on average 1% of the nominal prediction across all analysis bins.

Jet mismodeling: A discrepancy between the simulations and data was observed in some of the diboson CRs for high jet multiplicities. This is due to a mismodeling in QCD radiation. An additional uncertainty derived from the difference between the data and simulation in each jet bin in this CR is added to cover this discrepancy. The uncertainty is treated as correlated across jet bins. The uncertainty in the jet mismodeling is on average 7% of the nominal prediction across all analysis bins.

For the majority of the WCs studied in this analysis, the precision of the result is dominated by the statistical uncertainty; the systematic uncertainties represent the dominant contribution for six of the WCs, including two WCs from the 2hq2lq category (c_{Qq}^{18} and c_{tq}^{8}) as well as four WCs from the 2hqV category ($c_{\mathrm{t}G}$, $c_{\mathrm{t}\varphi}$, $c_{\varphi Q}^{-}$, and $c_{\varphi\mathrm{t}}$). For all of the WCs that are dominated by systematic uncertainties, the NLO cross section uncertainties (to which the LO samples are normalized) represent the leading sources of uncertainty. While normalization uncertainties represent the leading systematic uncertainties, this does not imply that the EFT primarily impacts the normalization. As discussed in section 5.4, binning the events in each selection category according to a kinematical distribution significantly improves the sensitivity, confirming that many of the WCs indeed have strong impacts on the kinematical shapes. Rather, the fact that the leading systematic uncertainties are normalization uncertainties is a reflection of the fact that EFT may lead to small deviations

Systematic uncertainty	Average change in the yields
Integrated luminosity	1.6%
Jet energy scale and resolution	1%
b jet tagging scale factors	1%
Theoretical cross section	1–4% (QCD) 1% (PDF)
Renormalization and factorization scales	3%
Parton shower	1–2%
Additional radiation	7%
Electron and muon identification and isolation	2% (electron) 1% (muon)
Trigger efficiency	$\leq$1%
Pileup	1%
L1 prefiring	1%
Misidentified-lepton rate	3%
Charge misreconstruction rate	1%
Jet mismodeling	7%

Table 4. Summary of systematic uncertainties along with the average change in the SM prediction yields.

with respect to the SM. A precise modeling of the SM distribution is thus important for identifying potentially small deviations from the SM, not only in the normalization but also in shape. Other systematic uncertainties that often have relatively large impacts for these WCs include various uncertainties related to the modeling (e.g., ISR, FSR, $\mu_{\rm R}$, and the diboson jet mismodeling uncertainty). For the WCs that are dominated by systematic uncertainties, the uncertainty on the nonprompt-lepton contribution generally represents the leading experimental systematic uncertainty.

The shape variation due to the PDF uncertainty is measured by reweighting the spectra using 100 replica sets and variations in $\alpha_{\rm S}$. The total uncertainty is then measured using the recommendation in PDF4LHC [59]. This uncertainty had a negligible effect on the analysis, so it was not included.

9   Results

The number of observed events for all 178 bins is shown in figures 4, 5, and 6 separated by the different signal categories, with the expectation obtained by setting all WCs to their SM values of zero (prefit) or simultaneously fitting the 26 WCs and the NPs by minimizing the NLL (postfit). To visualize the relative yields across the categories, figure 7 combines the bins of the kinematic variables, resulting in a plot of jet multiplicity for each selection category. The hatched regions in the stacked plot and shaded regions in the ratio plot correspond to the total systematic uncertainty. We have quantified the level of agreement between data and the SM hypothesis using a saturated model. We obtain a p-value of 0.18, showing no significant discrepancies between the two.
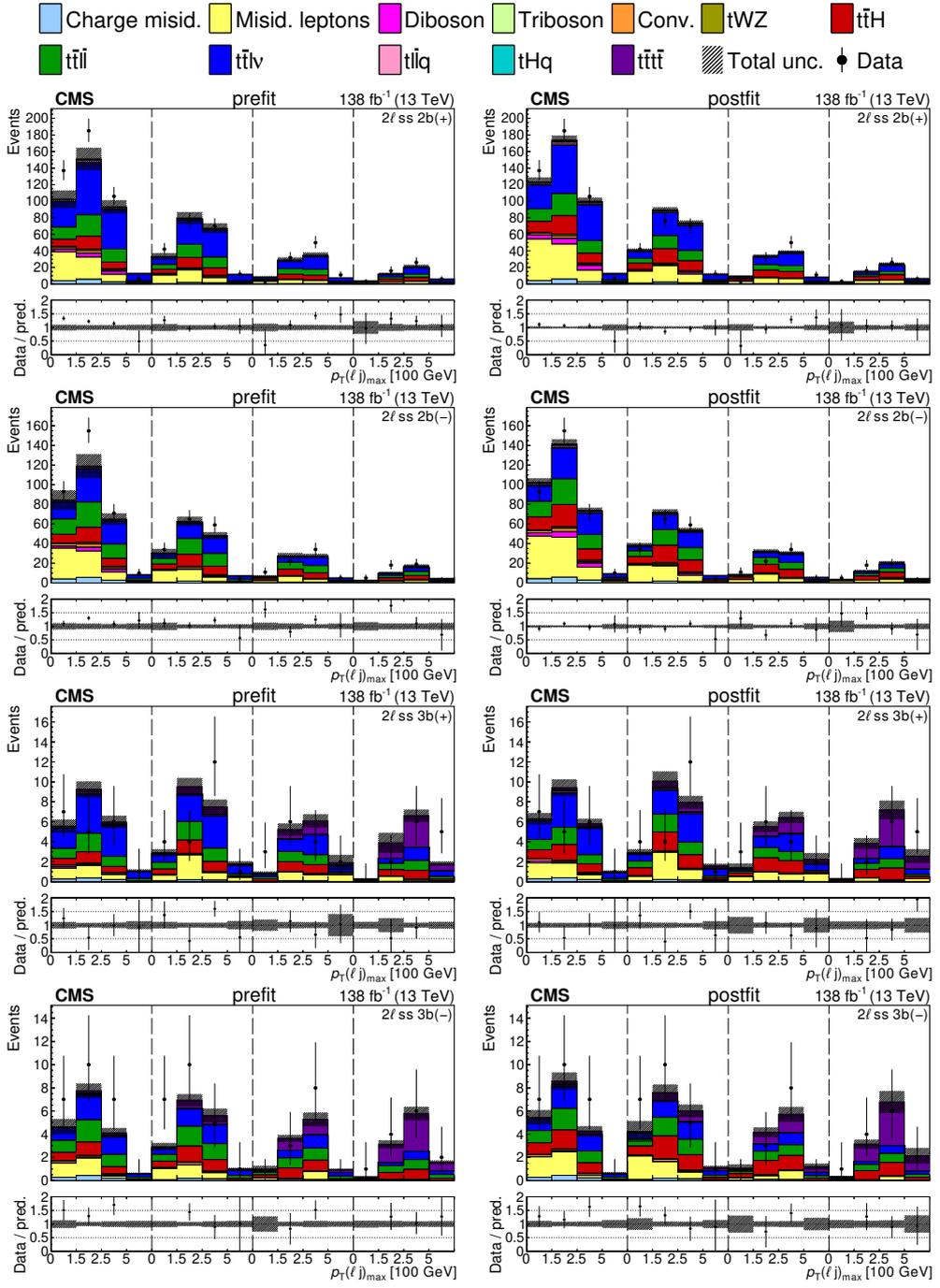
Figure 4. The categories shown in these plots are 2ℓss 2b and 2ℓss 3b. The prefit plots for each category are shown on the left side while the postfit plots are shown on the right side. The differential distribution in the plots is $p_{\mathrm{T}}(\ell\mathrm{j})_{\mathrm{max}}$. The jet subcategories are arranged from low jet multiplicity to high jet multiplicity from left to right for each individual plot. For example, in the 2ℓss 2b (+) plot, the first four bins are the $p_{\mathrm{T}}(\ell\mathrm{j})_{\mathrm{max}}$ variable for 2ℓss 2b (+) 4j, the next four bins are for 2ℓss 2b (+) 5j, etc. The process labeled "Conv." corresponds to the photon conversion background, "Misid. leptons" corresponds to misidentified leptons, and "Charge misid." corresponds to leptons with a mismeasured charge.
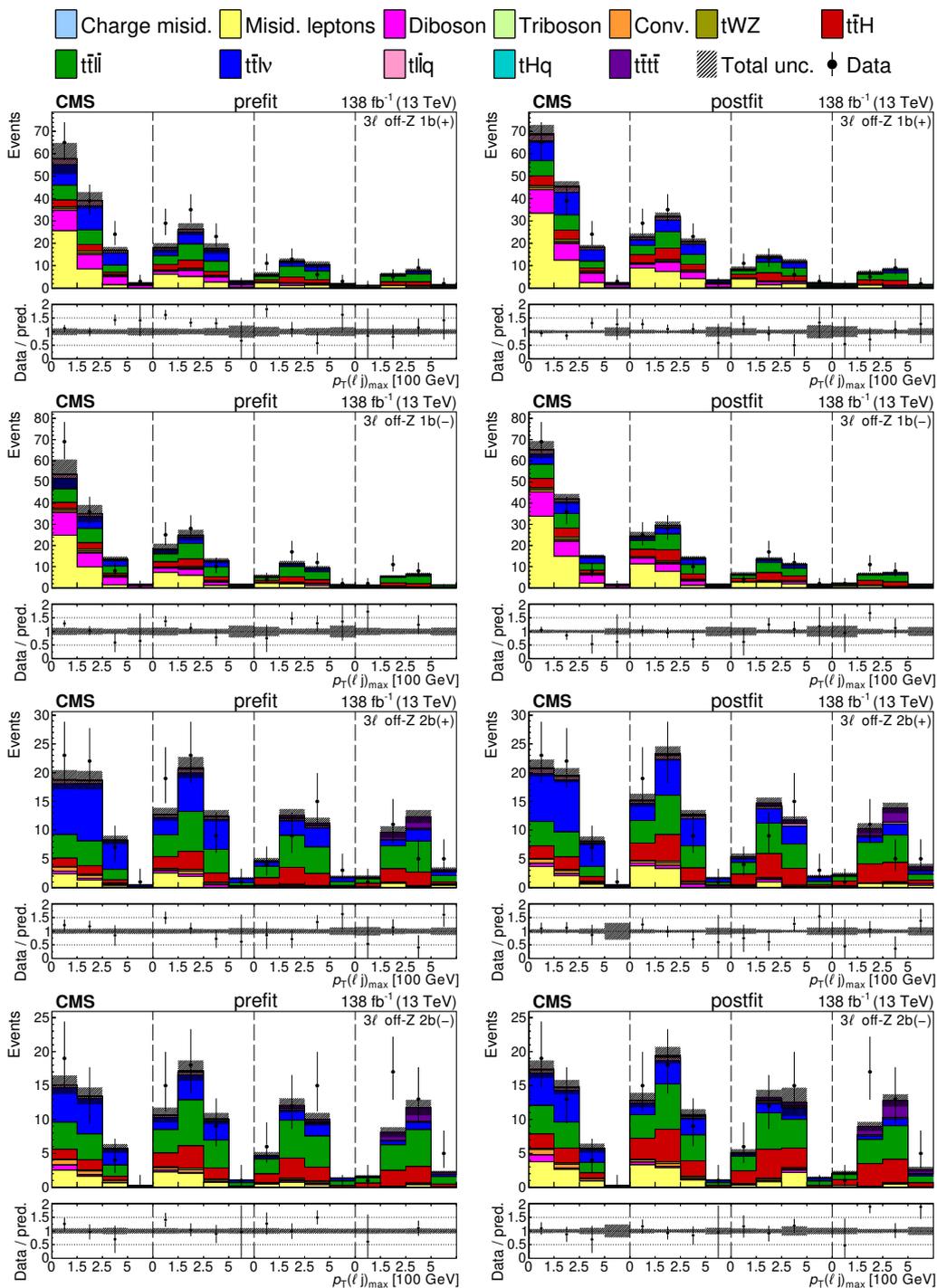
Figure 5. The categories shown in these plots are 3ℓ off-Z 1b and 3ℓ off-Z 2b. The prefit plots for each category are shown on the left side while the postfit plots are shown on the right side. The differential distribution in the plots is $p_T(\ell j)_{max}$. The jet subcategories are arranged from low jet multiplicity to high jet multiplicity from left to right for each individual plot. For example, in the 3ℓ off-Z 1b (+) plot, the first four bins are the $p_T(\ell j)_{max}$ variable for 3ℓ off-Z 1b (+) 2j, the next four bins are for 3ℓ off-Z 1b (+) 3j, etc.
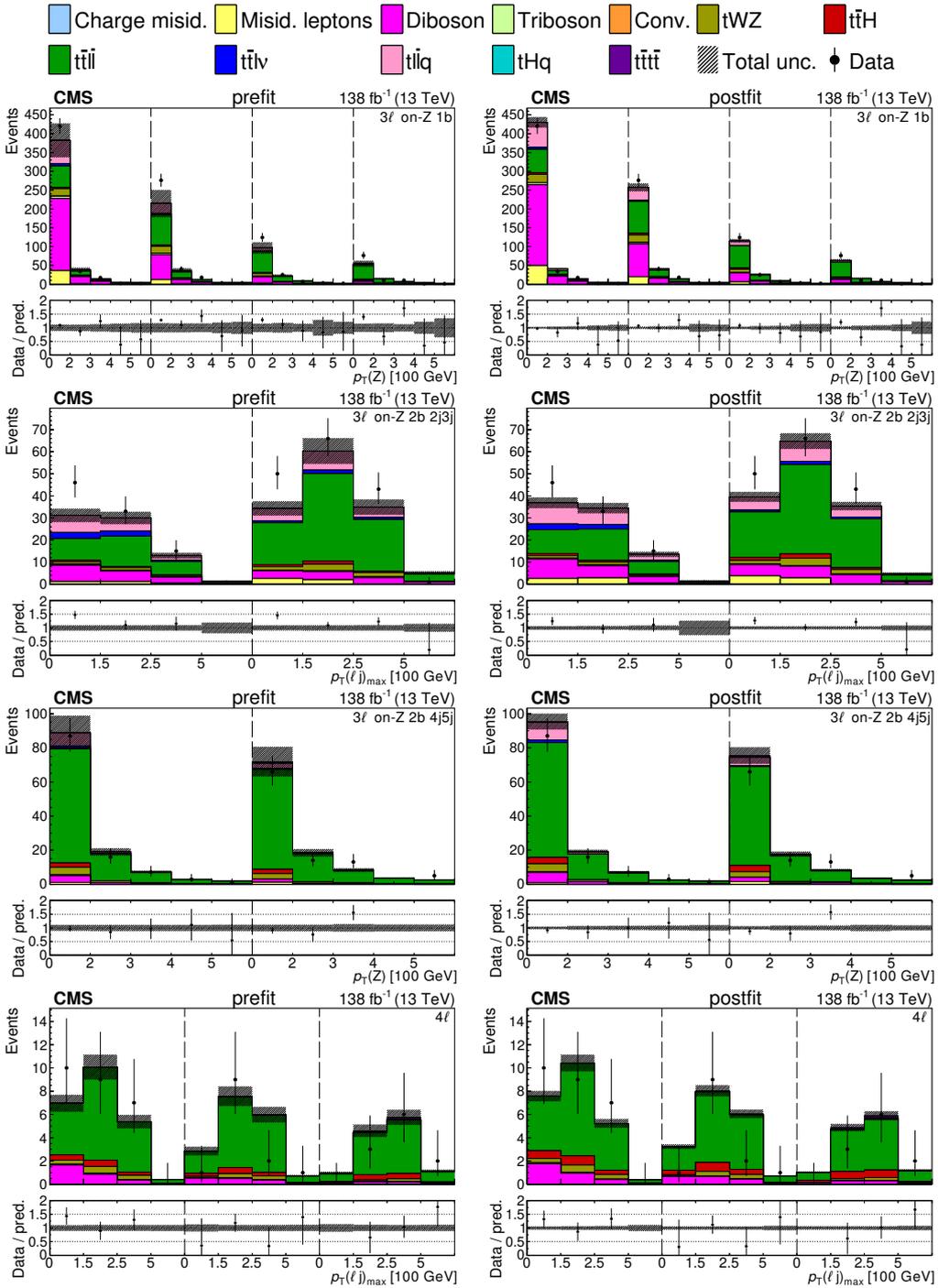
Figure 6. The categories shown in these plots are 3ℓ on-Z 1b, 3ℓ on-Z 2b, and 4ℓ. The prefit plots for each category are shown on the left side while the postfit plots are shown on the right side. The differential distribution is $p_T(Z)$ in the plots of 3ℓ on-Z 1b and 3ℓ on-Z 2b (4j and 5j), and $p_T(\ell j)_{max}$ in the plots of 3ℓ on-Z 2b (2j and 3j) and 4ℓ. The jet subcategories are arranged from low jet multiplicity to high jet multiplicity from left to right for each individual plot. For example, in the 3ℓ on-Z 1b plot, the first five bins are the $p_T(Z)$ variable for 3ℓ on-Z 2b 2j, the next five bins are for 3ℓ on-Z 2b 3j, etc.
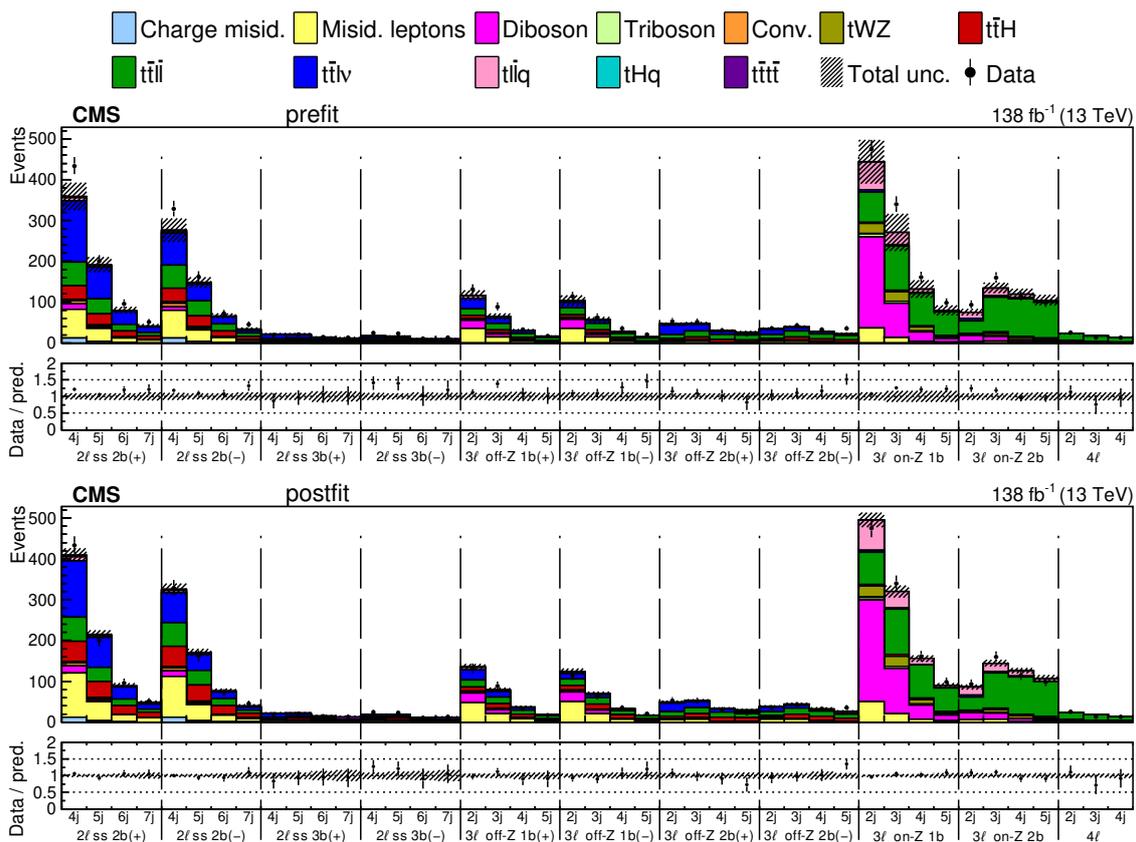
Figure 7. Observed data and expected yields in the prefit (upper) and postfit (lower) scenarios. All kinematic variables have been combined, resulting in distributions for the jet multiplicity only. The postfit values are obtained by simultaneously fitting all 26 Wilson coefficients (WCs) and the nuisance parameters (NPs). The lower panel contains the ratios of the observed yields over the expected. The error bands are computed by propagating the uncertainties from the WCs and NPs.

The 1 and 2σ CIs extracted from the likelihood fits described in section 7 are shown in figure 8. The solid black (dashed red) bars show the results of the fits in which the other 25 WCs are profiled (fixed to their SM values of zero). The CIs for all 26 WCs are consistent with the SM. The 1 and 2σ CIs for each WC are listed in tables 5 and 6, respectively. We note that, as mentioned in section 3, the definition of the operator associated with c_{tG} here includes an explicit factor of the strong coupling constant, which should be accounted for when comparing to results extracted based on other conventions.

The disjoint 1σ intervals that appear in some of the individual scans (i.e., the scans in which the other 25 WCs are fixed to zero) shown in figure 8 are a result of the quadratic nature of the EFT parametrization. In principle, this inherent degeneracy would apply for all WCs; however, the degeneracy can be broken when contributions from multiple processes in multiple bins result in one of the two minima having significantly better agreement with the observed data. The individual scans over the 4hq WCs are the only cases with a double minima that is sufficiently degenerate to lead to disjoint CIs. These double minima disappear when profiling over the other 25 WCs, since the interferences with the other
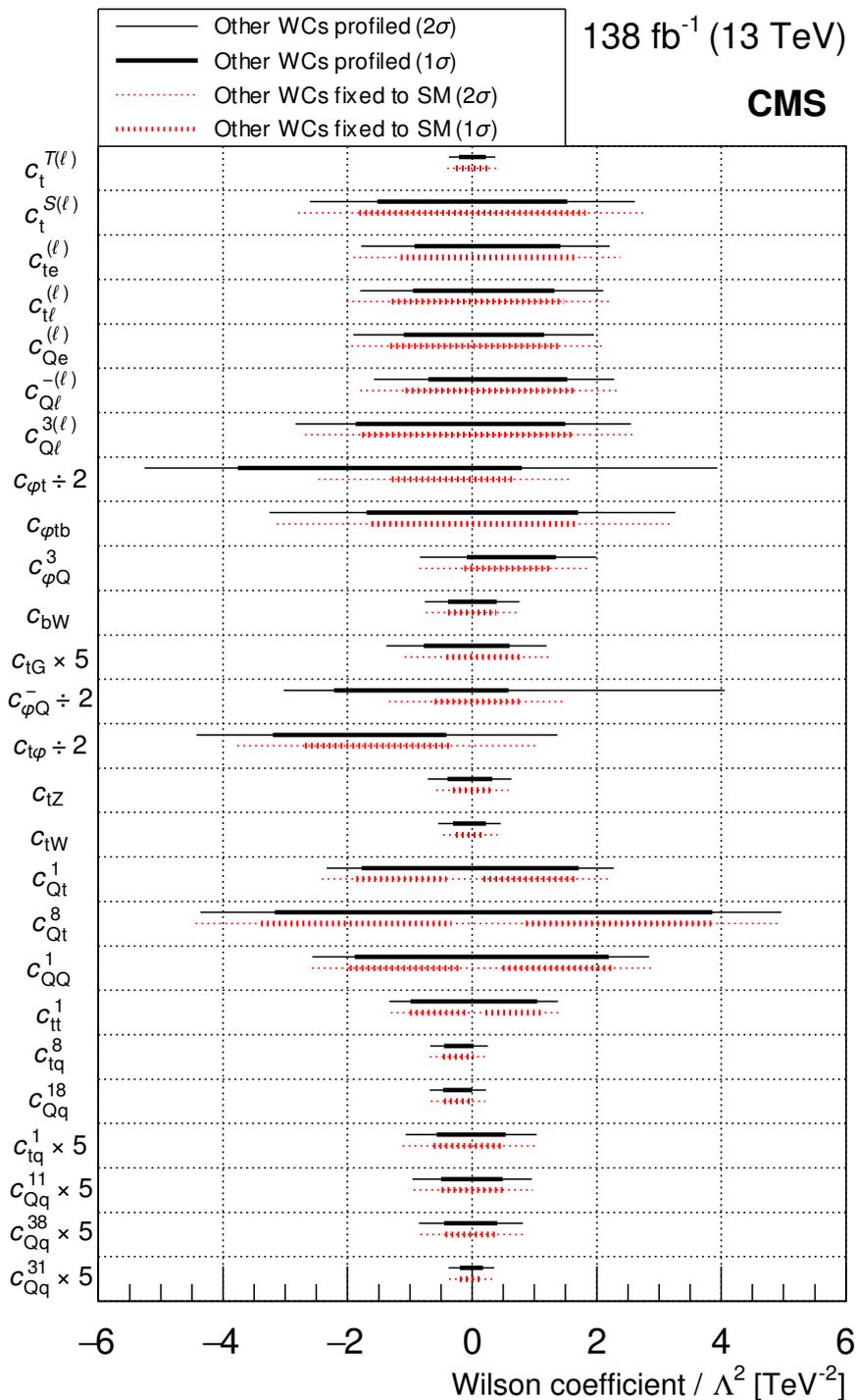
Figure 8. Summary of CIs extracted from the likelihood fits described in section 7. The WC 1σ (thick line) and 2σ (thin line) CIs are shown for the case where the other WCs are profiled (in solid black), and the case where the other WCs are fixed to their SM values of zero (in dashed red). To make the figure more readable, the intervals for $c_{t\varphi}$, $c_{\varphi t}$, and $c_{\varphi Q}^-$ were scaled by 0.5, and the intervals for c_{tG}, c_{tq}^1, c_{Qq}^{11}, c_{Qq}^{38}, and c_{Qq}^{31} were scaled by 5.

WC/Λ^2 [TeV^{-2}]	1σ CI (other WCs profiled)	1σ CI (other WCs fixed to SM)
WC category 2hq2ℓ		
$c_t^{T(\ell)}$	$[-0.22, 0.22]$	$[-0.26, 0.26]$
$c_t^{S(\ell)}$	$[-1.52, 1.53]$	$[-1.81, 1.82]$
$c_{te}^{(\ell)}$	$[-0.93, 1.41]$	$[-1.15, 1.68]$
$c_{t\ell}^{(\ell)}$	$[-0.95, 1.32]$	$[-1.29, 1.47]$
$c_{Qe}^{(\ell)}$	$[-1.10, 1.16]$	$[-1.32, 1.40]$
$c_{Q\ell}^{-(\ell)}$	$[-0.71, 1.53]$	$[-1.07, 1.64]$
$c_{Q\ell}^{3(\ell)}$	$[-1.87, 1.50]$	$[-1.76, 1.63]$
WC category 2hqV		
$c_{\varphi t}$	$[-7.52, 1.59]$	$[-2.59, 1.32]$
$c_{\varphi tb}$	$[-1.69, 1.70]$	$[-1.61, 1.67]$
$c_{\varphi Q}^3$	$[-0.09, 1.35]$	$[-0.13, 1.25]$
c_{bW}	$[-0.39, 0.40]$	$[-0.39, 0.39]$
c_{tG}	$[-0.15, 0.12]$	$[-0.08, 0.15]$
$c_{\varphi Q}^-$	$[-4.44, 1.17]$	$[-1.20, 1.57]$
$c_{t\varphi}$	$[-6.40, -0.82]$	$[-5.37, -0.64]$
c_{tZ}	$[-0.40, 0.32]$	$[-0.31, 0.32]$
c_{tW}	$[-0.31, 0.22]$	$[-0.26, 0.21]$
WC category 4hq		
c_{Qt}^1	$[-1.77, 1.71]$	$[-1.86, -0.41] \cup [0.19, 1.70]$
c_{Qt}^8	$[-3.17, 3.86]$	$[-3.39, -0.34] \cup [0.86, 3.87]$
c_{QQ}^1	$[-1.89, 2.19]$	$[-1.96, -0.16] \cup [0.49, 2.25]$
c_{tt}^1	$[-0.99, 1.05]$	$[-1.00, -0.08] \cup [0.21, 1.11]$
WC category 2hq2lq		
c_{tq}^8	$[-0.45, 0.03]$	$[-0.46, 0.02]$
c_{Qq}^{18}	$[-0.47, -0.00]$	$[-0.45, 0.00]$
c_{tq}^1	$[-0.11, 0.11]$	$[-0.12, 0.10]$
c_{Qq}^{11}	$[-0.10, 0.10]$	$[-0.10, 0.10]$
c_{Qq}^{38}	$[-0.09, 0.08]$	$[-0.09, 0.08]$
c_{Qq}^{31}	$[-0.04, 0.03]$	$[-0.04, 0.03]$

Table 5. The 1σ uncertainty intervals extracted from the likelihood fits described in section 7. The intervals are shown for the case where the other Wilson coefficients (WCs) are profiled, and the case where the other WCs are fixed to their SM values of zero.

WC/Λ^2 [TeV^{-2}]	2σ CI (other WCs profiled)	2σ CI (other WCs fixed to SM)
WC category 2hq2ℓ		
$c_{\mathrm{t}}^{T(\ell)}$	$[-0.37, 0.37]$	$[-0.40, 0.40]$
$c_{\mathrm{t}}^{S(\ell)}$	$[-2.60, 2.62]$	$[-2.80, 2.80]$
$c_{\mathrm{te}}^{(\ell)}$	$[-1.78, 2.21]$	$[-1.91, 2.39]$
$c_{\mathrm{t}\ell}^{(\ell)}$	$[-1.80, 2.11]$	$[-2.02, 2.20]$
$c_{Q\mathrm{e}}^{(\ell)}$	$[-1.91, 1.96]$	$[-2.04, 2.12]$
$c_{Q\ell}^{-(\ell)}$	$[-1.58, 2.28]$	$[-1.80, 2.33]$
$c_{Q\ell}^{3(\ell)}$	$[-2.84, 2.55]$	$[-2.69, 2.58]$
WC category 2hqV		
$c_{\varphi \mathrm{t}}$	$[-10.52, 7.87]$	$[-4.93, 3.18]$
$c_{\varphi \mathrm{tb}}$	$[-3.25, 3.26]$	$[-3.14, 3.18]$
$c_{\varphi Q}^{3}$	$[-0.84, 2.00]$	$[-0.85, 1.89]$
c_{bW}	$[-0.76, 0.76]$	$[-0.75, 0.75]$
$c_{\mathrm{t}G}$	$[-0.28, 0.24]$	$[-0.22, 0.25]$
$c_{\varphi Q}^{-}$	$[-6.06, 8.12]$	$[-2.68, 2.94]$
$c_{\mathrm{t}\varphi}$	$[-8.85, 2.75]$	$[-7.54, 2.11]$
c_{tZ}	$[-0.71, 0.64]$	$[-0.58, 0.59]$
c_{tW}	$[-0.55, 0.46]$	$[-0.47, 0.41]$
WC category 4hq		
$c_{Q\mathrm{t}}^{1}$	$[-2.34, 2.27]$	$[-2.41, 2.22]$
$c_{Q\mathrm{t}}^{8}$	$[-4.37, 4.97]$	$[-4.45, 4.96]$
c_{QQ}^{1}	$[-2.56, 2.84]$	$[-2.57, 2.89]$
c_{tt}^{1}	$[-1.33, 1.38]$	$[-1.31, 1.43]$
WC category 2hq2lq		
c_{tq}^{8}	$[-0.68, 0.25]$	$[-0.68, 0.24]$
$c_{Q\mathrm{q}}^{18}$	$[-0.68, 0.22]$	$[-0.67, 0.21]$
c_{tq}^{1}	$[-0.21, 0.21]$	$[-0.22, 0.20]$
$c_{Q\mathrm{q}}^{11}$	$[-0.19, 0.19]$	$[-0.19, 0.20]$
$c_{Q\mathrm{q}}^{38}$	$[-0.17, 0.16]$	$[-0.17, 0.16]$
$c_{Q\mathrm{q}}^{31}$	$[-0.08, 0.07]$	$[-0.08, 0.07]$

Table 6. The 2σ uncertainty intervals extracted from the likelihood fits described in section 7. The intervals are shown for the case where the other Wilson coefficients (WCs) are profiled, and the case where the other WCs are fixed to their SM values of zero.

WCs can compensate for one another's effects within the range between the two minima, resulting in a single long, flat minimum instead of two disjoint minima. Double minima in the individual scans (even relatively shallow double minima that do not manifest in disjoint CIs) can broaden the CI interval and sometimes lead to individual CIs that are wider than the corresponding profiled CIs, as described in ref. [12]. For many of the WCs, the CIs obtained from the profiled and individual scans are similar; for some of the WCs, this results from the fact that there are not significant correlations between the given WC and the other WCs. However, in other cases there are non-trivial correlations among several of the WCs, and this will be explored further in section 9.1.

Performing the likelihood fit over all 26 WCs simultaneously, this work supersedes ref. [12] as the most global detector-level EFT analysis to date. Not only does this work incorporate 10 additional WCs that were not studied in ref. [12], but it also obtains significantly improved constraints on the WCs. For the WCs that are common between the analyses, the 2σ profiled CIs generally improve by factors of approximately 2 to 6, depending on the WC. The differential approach leveraged by this analysis provides the majority of the improvement, though the larger data set also helps to increase the sensitivity.

9.1 Two-dimensional correlations among WCs

To explore correlations among the WCs in the 26-dimensional fit, this section presents 2D scans for several pairs of WCs with nonnegligible correlations. These pairs include several from the 2hqV category of WCs (shown in figures 9–10) and several from the 4hq category of WCs (shown in figure 11). In most cases, the 2D scans in which the other 24 WCs are profiled are very similar to the 2D scans in which the other WCs are fixed to zero, indicating that while the correlations between the given pair of WCs are important, the correlations with the other 24 are less significant. For example, figure 9 shows a 2D scan over the c_{tZ} and c_{tW} WCs with the other 24 WCs fixed to their SM values of zero (on the left) or profiled (on the right); while a strong correlation between c_{tZ} and c_{tW} is evident, the other 24 WCs are not significantly correlated with either of these two WCs. Figure 10 shows correlations between other 2hqV WCs. Two disjoint contours of the 2σ CI are visible in the 2D scan over $c_{t\varphi}$ and c_{tG} in the right-hand side of this figure; the confidence intervals shown in figure 8 do not have two disjoint intervals because the minimum is not deep enough to cross the 2σ threshold in the one-dimensional scan. Pairs of WCs from the 4hq category are shown in figure 11. Near the SM, where their interference terms compensate for one another as discussed above, these four WCs have significant correlations with each other. However, farther from the SM at the 1 and 2σ limits, the quadratic terms dominate over the linear terms, so the effects of all WCs monotonically increase the yields; for this reason, the WCs can no longer compensate for each other, so they become uncorrelated in the fit. This is why the contour plots in figure 11 show minimal correlations between the pairs of WCs.

9.2 Interpretation of sensitivity

In this section, we discuss the sensitivity to the WCs (which is quantified by the CIs), focusing on the likelihood fits with other WCs profiled. While all 178 analysis bins contribute
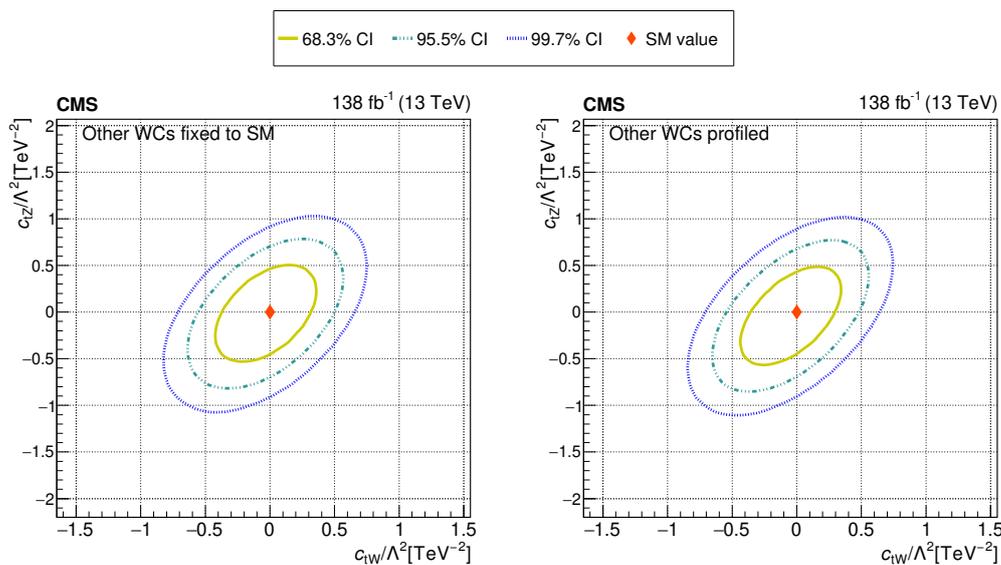
Figure 9. The observed 68.3, 95.5, and 99.7% confidence level contours of a 2D scan for c_{tW} and c_{tZ} with the other WCs fixed to their SM values (left), and profiled (right). Diamond markers show the SM prediction.
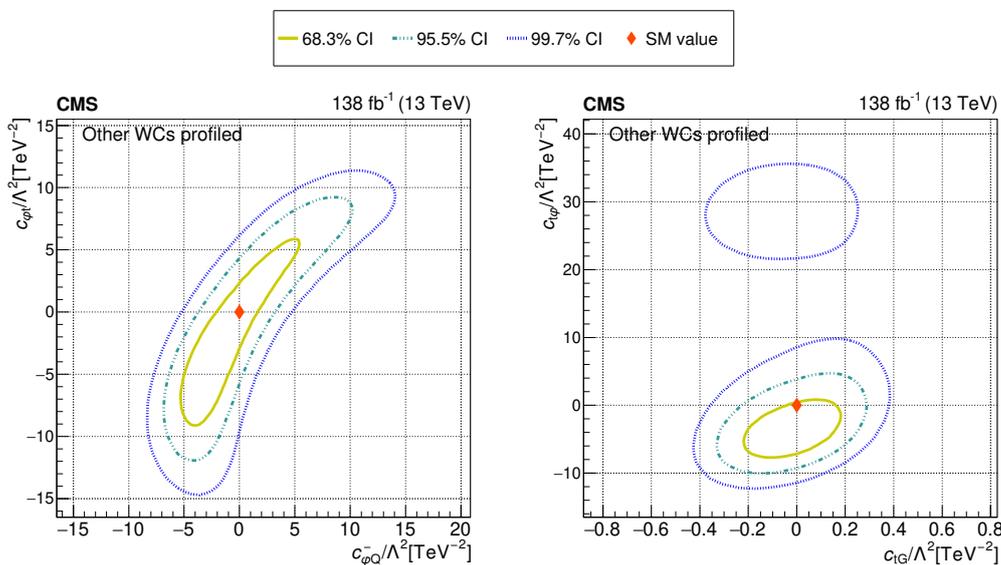
Figure 10. The observed 68.3, 95.5, and 99.7% confidence level contours of a 2D scan with the other WCs profiled, for $c_{\varphi Q}^{-}$ and $c_{\varphi \mathrm{t}}$ (left), and for $c_{\mathrm{t}G}$ and $c_{\mathrm{t}\varphi}$ (right). Diamond markers show the SM prediction.
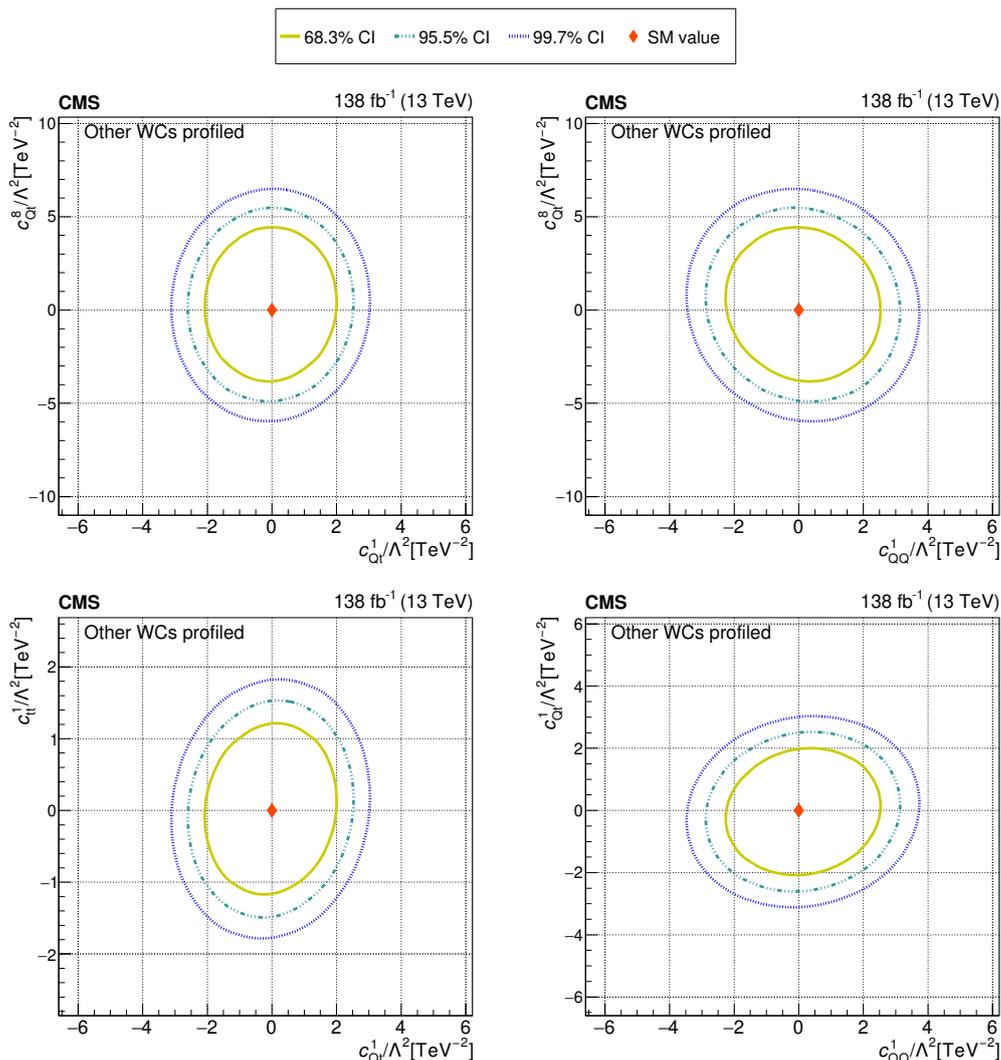
Figure 11. The observed 68.3, 95.5, and 99.7% confidence level contours of a 2D scan with the other WCs profiled, for c^1_{Qt} and c^8_{Qt} (upper left), for c^1_{QQ} and c^8_{Qt} (upper right), for c^1_{Qt} and c^1_{tt} (lower left), and for c^1_{QQ} and c^1_{Qt} (lower right). Diamond markers show the SM prediction.

to the sensitivity to the 26 WCs, the relative contribution of each bin varies by WC. Organizing the WCs based primarily on the interactions they modify and the processes they most strongly impact, the WCs may be classified into seven main groups, summarized in table 7. The WCs that belong to each grouping are listed in the center column of table 7, while the right-hand column notes the category (or categories) of analysis bins that generally provide the leading sensitivity to the WCs in the given group. It should be emphasized that the categories of bins listed in the right-hand column of table 7 represent a simplified picture of the interpretation of the sensitivity: while there are indeed some cases where the majority of the sensitivity to a WC is derived from a relatively clear subset of the analysis bins, the sensitivity to many of the WCs is provided by a diverse combination of bins across all selection categories. Furthermore, when characterizing relevant bins, it is

Grouping of WCs	WCs	Lead categories
2hq2ℓ	$c_{Q\ell}^{3(\ell)}$, $c_{Q\ell}^{-(\ell)}$, $c_{Qe}^{(\ell)}$, $c_{t\ell}^{(\ell)}$, $c_{te}^{(\ell)}$, $c_{t}^{S(\ell)}$, $c_{t}^{T(\ell)}$	3ℓ off-Z
4hq	c_{QQ}^1, c_{Qt}^1, c_{Qt}^8, c_{tt}^1	2ℓss
2hq2lq "$t\bar{t}\ell\nu$-like"	c_{Qq}^{11}, c_{Qq}^{18}, c_{tq}^1, c_{tq}^8	2ℓss
2hq2lq "$t\ell\bar{\ell}$q-like"	c_{Qq}^{31}, c_{Qq}^{38}	3ℓ on-Z
2hqV "$t\bar{t}\ell\bar{\ell}$-like"	c_{tZ}, $c_{\varphi t}$, $c_{\varphi Q}^-$	3ℓ on-Z and 2ℓss
2hqV "tXq-like"	$c_{\varphi Q}^3$, $c_{\varphi tb}$, c_{bW}	3ℓ on-Z
2hqV (significant impacts on many processes)	c_{tG}, $c_{t\varphi}$, c_{tW}	3ℓ and 2ℓss

Table 7. Summary of categories that provide leading contributions to the sensitivity for subsets of the Wilson coefficients (WCs).

also important to keep in mind interference and correlations among WCs. The following subsections will step through each of the groups of WCs outlined in table 7, discussing the subsets of bins that provide the leading contributions to the sensitivity and discussing non-trivial correlations where relevant.

9.2.1 The WCs from the 2hq2ℓ category of operators

Beginning with the WCs in the 2hq2ℓ group, the 3ℓ off-Z channels provide the majority of the sensitivity for these WCs, which are associated with four-fermion vertices that produce pairs of leptons without an intermediate Z boson. To quantify the contributions of the off-Z channels, a fit is performed with only this subset of bins included. The resulting 2σ profiled CIs show that the expected sensitivity is only degraded by about 5–7% compared to the results when all bins are included.

9.2.2 The WCs from the 4hq category of operators

The next group of WCs are those associated with the 4hq operators. The sensitivity to these WCs is provided primarily by the 2ℓss bins, with leading contributions from the bins requiring at least three b-tagged jets. Since the $t\bar{t}t\bar{t}$ process contributes significantly to these bins and the four-heavy WCs strongly affect the $t\bar{t}t\bar{t}$ process (both the total cross section and shape of the kinematic distributions), it is expected that these bins would contribute significantly to the sensitivity. To obtain a quantitative characterization of the sensitivity provided by the 2ℓss bins, we performed a fit with only these bins included. The resulting 2σ CIs are only degraded by about 4–6% (with respect to a fit with all bins included), showing that the 2ℓss bins indeed represent the dominant source of sensitivity to the four-heavy WCs.

9.2.3 The WCs from the 2hq2lq category of operators

The next set of WCs are those associated with the 2hq2lq category of operators. Four of these WCs (c_{Qq}^{11}, c_{tq}^{1}, c_{Qq}^{18}, and c_{tq}^{8}) primarily affect the $t\bar{t}\ell\nu$ process, so bins populated significantly by $t\bar{t}\ell\nu$ are expected to provide important contributions to the sensitivity to these WCs. Performing a fit with only the 2ℓss bins included, the expected 2σ CIs are degraded by only about 6–15%. The 2ℓss bins thus provide the primary source of sensitivity for these WCs, though other bins (e.g., from the off-Z channels) also contribute to the sensitivity.

The remaining two WCs from the 2hq2lq group (c_{Qq}^{31} and c_{Qq}^{38}) are distinct from the other 2hq2lq WCs in that they feature tbqq$'$ vertices. These vertices allow c_{Qq}^{31} and c_{Qq}^{38} to significantly impact the $t\ell\bar{\ell}q$ process in the 3ℓ on-Z bins with two b-tagged jets and low jet multiplicity (as discussed in section 5.4). The on-Z bins thus contribute significant sensitivity to these WCs. While the 2ℓss and off-Z categories also contribute to the sensitivity to these WCs, the 3ℓ on-Z bins provide the leading contribution. The expected 2σ CIs for these WCs each widen by more than 30% when the 3ℓ on-Z bins are excluded from the fit.

9.2.4 The WCs from the 2hqV category of operators

The final set of WCs are those associated with the 2hqV category of operators. These nine WCs impact a broad range of processes, leading to diverse effects across the full set of 178 analysis bins and making it challenging to definitively characterize subsets of bins that provide dominant contributions to the sensitivity. However, the WCs can be classified into three main groups (as listed in table 7) based on the processes they impact most significantly.

The c_{tZ}, $c_{\varphi Q}^{-}$, and $c_{\varphi t}$ WCs feature $t\bar{t}Z$ EFT vertices and primarily affect the $t\bar{t}\ell\bar{\ell}$ process; the on-Z bins are thus important for these WCs. However, these WCs also impact other processes (e.g., $t\bar{t}t\bar{t}$), meaning other categories of bins can also provide important sensitivity. Furthermore, the $t\bar{t}\ell\bar{\ell}$ process also significantly populates the 2ℓss bins (making up about 20% of the total expected yield), so the $t\bar{t}\ell\bar{\ell}$ effects can also be relevant in the 2ℓss bins. Thus, the 3ℓ on-Z bins and 2ℓss bins are important for these WCs. The 3ℓ off-Z bins provide a smaller (though nonzero) contribution to the sensitivity. Performing a fit with these bins excluded results in an approximately 6% degradation of the expected 2σ CIs for each of these three WCs.

Next, let us consider $c_{\varphi Q}^{3}$, $c_{\varphi \mathrm{tb}}$, and c_{bW}. These WCs primarily impact $t\ell\bar{\ell}q$ and tHq, and their sensitivity arises from multiple categories of analysis bins. The 3ℓ on-Z bins represent the leading (though not overwhelmingly dominant) contribution. Performing a fit with only the 3ℓ on-Z bins included, the expected 2σ CIs for these WCs widen by about 2–13% (depending on the WC) compared to a fit with all bins included.

The final three WCs from the 2hqV group are $c_{\mathrm{t}G}$, $c_{\mathrm{t}\varphi}$, and c_{tW}. Impacting multiple processes, these WCs gain sensitivity from the full spectrum of analysis bins. For example, $c_{\mathrm{t}G}$ impacts $t\bar{t}H$ (so the 2ℓss and 3ℓ off-Z bins are important as $t\bar{t}H$ significantly populates these bins) but also strongly impacts $t\bar{t}\ell\bar{\ell}$ (so the on-Z and 2ℓss bins also play an important role). The $c_{\mathrm{t}\varphi}$ WC significantly impacts $t\bar{t}H$, tHq, and $t\bar{t}t\bar{t}$; most of the analysis bins provide sensitivity to this WC, though the on-Z bins provide only minor contributions

(dropping the on-Z bins only results in about a 5% effect on the expected 2σ profiled CIs for $c_{t\varphi}$). Finally, the c_{tW} WC impacts all signal processes and derives important sensitivity from many of the analysis bins. Further complicating the picture, c_{tW} has significant interference with c_{tZ}, and the two WCs have a strong linear correlation in the profiled fit (as shown in figure 9). Thus, when we consider the 2σ profiled CIs for c_{tW}, it is important to recall that the c_{tZ} operator is also set to a nonzero value, so bins that are affected by c_{tZ} can also be important when considering the sensitivity to c_{tW}.

10 Summary

A search for new physics in the production of one or more top quarks with additional leptons, jets, and b jets in the context of effective field theory (EFT) has been performed. Events from proton-proton collisions with a center-of-mass energy of $13\,\mathrm{TeV}$ corresponding to an integrated luminosity of $138\,\mathrm{fb}^{-1}$ are used. EFT effects are incorporated into the event weights of the simulated samples, allowing detector-level predictions that account for correlations and interference effects among EFT operators and between EFT operators and standard model (SM) processes.

The Wilson coefficients (WCs) corresponding to 26 EFT operators were simultaneously fit to the data. Confidence intervals were extracted for the WCs either individually or in pairs by scanning the likelihood with the other WCs either profiled or fixed at their SM values of zero. In all cases, the data are found to be consistent with the SM expectations.

Acknowledgments

References

[1] J.L. Feng, *Dark matter candidates from particle physics and methods of detection*, *Ann. Rev. Astron. Astrophys.* **48** (2010) 495 [`arXiv:1003.0904`] [INSPIRE].

[2] T.A. Porter, R.P. Johnson and P.W. Graham, *Dark matter searches with astroparticle data*, *Ann. Rev. Astron. Astrophys.* **49** (2011) 155 [`arXiv:1104.2836`] [INSPIRE].

[3] C. Degrande et al., *Effective field theory: a modern approach to anomalous couplings*, *Annals Phys.* **335** (2013) 21 [arXiv:1205.4231] [INSPIRE].

[4] CDF collaboration, *Observation of top quark production in $\bar{p}p$ collisions*, *Phys. Rev. Lett.* **74** (1995) 2626 [hep-ex/9503002] [INSPIRE].

[5] D0 collaboration, *Observation of the top quark*, *Phys. Rev. Lett.* **74** (1995) 2632 [hep-ex/9503003] [INSPIRE].

[6] PARTICLE DATA GROUP collaboration, *Review of particle physics*, *PTEP* **2022** (2022) 083C01 [INSPIRE].

[7] CMS collaboration, *Measurement of the Higgs boson production rate in association with top quarks in final states with electrons, muons, and hadronically decaying tau leptons at $\sqrt{s} = 13\,TeV$*, *Eur. Phys. J. C* **81** (2021) 378 [arXiv:2011.03652] [INSPIRE].

[8] CMS collaboration, *Measurement of the cross section of top quark-antiquark pair production in association with a W boson in proton-proton collisions at $\sqrt{s} = 13\,TeV$*, *JHEP* **07** (2023) 219 [arXiv:2208.06485] [INSPIRE].

[9] CMS collaboration, *Measurement of top quark pair production in association with a Z boson in proton-proton collisions at $\sqrt{s} = 13\,TeV$*, *JHEP* **03** (2020) 056 [arXiv:1907.11270] [INSPIRE].

[10] CMS collaboration, *Inclusive and differential cross section measurements of single top quark production in association with a Z boson in proton-proton collisions at $\sqrt{s} = 13\,TeV$*, *JHEP* **02** (2022) 107 [arXiv:2111.02860] [INSPIRE].

[11] CMS collaboration, *Evidence for four-top quark production in proton-proton collisions at $\sqrt{s} = 13\,TeV$*, *Phys. Lett. B* **844** (2023) 138076 [arXiv:2303.03864] [INSPIRE].

[12] CMS collaboration, *Search for new physics in top quark production with additional leptons in proton-proton collisions at $\sqrt{s} = 13\,TeV$ using effective field theory*, *JHEP* **03** (2021) 095 [arXiv:2012.04120] [INSPIRE].

[13] CMS collaboration, *Probing effective field theory operators in the associated production of top quarks with a Z boson in multilepton final states at $\sqrt{s} = 13\,TeV$*, *JHEP* **12** (2021) 083 [arXiv:2107.13896] [INSPIRE].

[14] CMS collaboration, *Search for new physics using effective field theory in 13 TeV pp collision events that contain a top quark pair and a boosted Z or Higgs boson*, *Phys. Rev. D* **108** (2023) 032008 [arXiv:2208.12837] [INSPIRE].

[15] *HEPData record for this analysis*, CMS-TOP-22-006 (2023).

[16] CMS collaboration, *The CMS experiment at the CERN LHC*, 2008 *JINST* **3** S08004 [INSPIRE].

[17] CMS collaboration, *Performance of the CMS level-1 trigger in proton-proton collisions at $\sqrt{s} = 13\,TeV$*, 2020 *JINST* **15** P10017 [arXiv:2006.10165] [INSPIRE].

[18] CMS collaboration, *The CMS trigger system*, 2017 *JINST* **12** P01020 [arXiv:1609.02366] [INSPIRE].

[19] J. Alwall et al., *The automated computation of tree-level and next-to-leading order differential cross sections, and their matching to parton shower simulations*, *JHEP* **07** (2014) 079 [arXiv:1405.0301] [INSPIRE].

[20] R. Frederix and S. Frixione, *Merging meets matching in MC@NLO*, *JHEP* **12** (2012) 061 [arXiv:1209.6215] [InSPIRE].

[21] J. Alwall et al., *Comparative study of various algorithms for the merging of parton showers and matrix elements in hadronic collisions*, *Eur. Phys. J. C* **53** (2008) 473 [arXiv:0706.2569] [InSPIRE].

[22] D. Barducci et al., *Interpreting top-quark LHC measurements in the standard-model effective field theory*, arXiv:1802.07237 [InSPIRE].

[23] B. Grzadkowski, M. Iskrzynski, M. Misiak and J. Rosiek, *Dimension-six terms in the standard model Lagrangian*, *JHEP* **10** (2010) 085 [arXiv:1008.4884] [InSPIRE].

[24] R. Goldouzian et al., *Matching in $pp \to t\bar{t}W/Z/h + jet$ SMEFT studies*, *JHEP* **06** (2021) 151 [arXiv:2012.06872] [InSPIRE].

[25] NNPDF collaboration, *Parton distributions for the LHC run II*, *JHEP* **04** (2015) 040 [arXiv:1410.8849] [InSPIRE].

[26] T. Sjöstrand, S. Mrenna and P.Z. Skands, *A brief introduction to PYTHIA* 8.1, *Comput. Phys. Commun.* **178** (2008) 852 [arXiv:0710.3820] [InSPIRE].

[27] CMS collaboration, *Extraction and validation of a new set of CMS PYTHIA8 tunes from underlying-event measurements*, *Eur. Phys. J. C* **80** (2020) 4 [arXiv:1903.12179] [InSPIRE].

[28] LHC HIGGS CROSS SECTION WORKING GROUP collaboration, *Handbook of LHC Higgs cross sections: 4. Deciphering the nature of the Higgs sector*, arXiv:1610.07922 [DOI:10.23731/CYRM-2017-002] [InSPIRE].

[29] R. Frederix and I. Tsinikos, *On improving NLO merging for $t\bar{t}W$ production*, *JHEP* **11** (2021) 029 [arXiv:2108.07826] [InSPIRE].

[30] M. van Beekveld, A. Kulesza and L.M. Valero, *Threshold resummation for the production of four top quarks at the LHC*, *Phys. Rev. Lett.* **131** (2023) 211901 [arXiv:2212.03259] [InSPIRE].

[31] O. Mattelaer, *On the maximal use of Monte Carlo samples: re-weighting events at NLO accuracy*, *Eur. Phys. J. C* **76** (2016) 674 [arXiv:1607.00763] [InSPIRE].

[32] CMS collaboration, *Particle-flow reconstruction and global event description with the CMS detector*, 2017 *JINST* **12** P10003 [arXiv:1706.04965] [InSPIRE].

[33] CMS collaboration, *Electron and photon reconstruction and identification with the CMS experiment at the CERN LHC*, 2021 *JINST* **16** P05014 [arXiv:2012.06888] [InSPIRE].

[34] CMS collaboration, *ECAL 2016 refined calibration and Run2 summary plots*, CMS-DP-2020-021, CERN, Geneva, Switzerland (2020).

[35] CMS collaboration, *Performance of the CMS muon detector and muon reconstruction with proton-proton collisions at $\sqrt{s} = 13$ TeV*, 2018 *JINST* **13** P06015 [arXiv:1804.04528] [InSPIRE].

[36] CMS collaboration, *Identification of prompt and isolated muons using multivariate techniques at the CMS experiment in proton-proton collisions at $\sqrt{s} = 13$ TeV*, CMS-PAS-MUO-22-001, CERN, Geneva, Switzerland (2023).

[37] M. Cacciari, G.P. Salam and G. Soyez, *The anti-k_t jet clustering algorithm*, *JHEP* **04** (2008) 063 [arXiv:0802.1189] [InSPIRE].

[38] M. Cacciari, G.P. Salam and G. Soyez, *FastJet user manual*, *Eur. Phys. J. C* **72** (2012) 1896 [arXiv:1111.6097] [INSPIRE].

[39] CMS collaboration, *Pileup mitigation at CMS in* 13 *TeV data*, 2020 *JINST* **15** P09018 [arXiv:2003.00503] [INSPIRE].

[40] CMS collaboration, *Jet energy scale and resolution in the CMS experiment in pp collisions at* 8 *TeV*, 2017 *JINST* **12** P02014 [arXiv:1607.03663] [INSPIRE].

[41] CMS collaboration, *Identification of heavy-flavour jets with the CMS detector in pp collisions at* 13 *TeV*, 2018 *JINST* **13** P05011 [arXiv:1712.07158] [INSPIRE].

[42] E. Bols et al., *Jet flavour classification using DeepJet*, 2020 *JINST* **15** P12012 [arXiv:2008.10519] [INSPIRE].

[43] CMS collaboration, *Performance summary of AK4 jet b tagging with data from proton-proton collisions at* 13 *TeV with the CMS detector*, CMS-DP-2023-005, CERN, Geneva, Switzerland (2023).

[44] P. Nason, *A new method for combining NLO QCD with shower Monte Carlo algorithms*, *JHEP* **11** (2004) 040 [hep-ph/0409146] [INSPIRE].

[45] S. Frixione, P. Nason and C. Oleari, *Matching NLO QCD computations with parton shower simulations: the POWHEG method*, *JHEP* **11** (2007) 070 [arXiv:0709.2092] [INSPIRE].

[46] S. Alioli, P. Nason, C. Oleari and E. Re, *A general framework for implementing NLO calculations in shower Monte Carlo programs: the POWHEG BOX*, *JHEP* **06** (2010) 043 [arXiv:1002.2581] [INSPIRE].

[47] T. Melia, P. Nason, R. Rontsch and G. Zanderighi, W^+W^-, WZ and ZZ production in the POWHEG BOX, *JHEP* **11** (2011) 078 [arXiv:1107.5051] [INSPIRE].

[48] S. Frixione, P. Nason and G. Ridolfi, *A positive-weight next-to-leading-order Monte Carlo for heavy flavour hadroproduction*, *JHEP* **09** (2007) 126 [arXiv:0707.3088] [INSPIRE].

[49] J.M. Campbell and R.K. Ellis, *An update on vector boson pair production at hadron colliders*, *Phys. Rev. D* **60** (1999) 113006 [hep-ph/9905386] [INSPIRE].

[50] M. Grazzini et al., *NNLO QCD + NLO EW with Matrix+OpenLoops: precise predictions for vector-boson pair production*, *JHEP* **02** (2020) 087 [arXiv:1912.00068] [INSPIRE].

[51] F. Caola, K. Melnikov, R. Röntsch and L. Tancredi, *QCD corrections to ZZ production in gluon fusion at the LHC*, *Phys. Rev. D* **92** (2015) 094028 [arXiv:1509.06734] [INSPIRE].

[52] CMS collaboration, *Search for electroweak production of charginos and neutralinos in multilepton final states in proton-proton collisions at* $\sqrt{s} = 13$ *TeV*, *JHEP* **03** (2018) 166 [arXiv:1709.05406] [INSPIRE].

[53] W. Verkerke and D.P. Kirkby, *The RooFit toolkit for data modeling*, *eConf* **C0303241** (2003) MOLT007 [physics/0306116] [INSPIRE].

[54] CMS collaboration, *Precision luminosity measurement in proton-proton collisions at* $\sqrt{s} = 13$ *TeV in* 2015 *and* 2016 *at CMS*, *Eur. Phys. J. C* **81** (2021) 800 [arXiv:2104.01927] [INSPIRE].

[55] CMS collaboration, *CMS luminosity measurement for the* 2017 *data-taking period at* $\sqrt{s} = 13$ *TeV*, CMS-PAS-LUM-17-004, CERN, Geneva, Switzerland (2018).

[56] CMS collaboration, *CMS luminosity measurement for the* 2018 *data-taking period at* $\sqrt{s} = 13$ *TeV*, CMS-PAS-LUM-18-002, CERN, Geneva, Switzerland (2019).

[57] CMS collaboration, *Measurements of inclusive W and Z cross sections in pp collisions at* $\sqrt{s} = 7$ *TeV*, *JHEP* **01** (2011) 080 [`arXiv:1012.2466`] [INSPIRE].

[58] CMS collaboration, *Measurement of the inelastic proton-proton cross section at* $\sqrt{s} = 13$ *TeV*, *JHEP* **07** (2018) 161 [`arXiv:1802.02613`] [INSPIRE].

[59] J. Butterworth et al., *PDF4LHC recommendations for LHC run II*, *J. Phys. G* **43** (2016) 023001 [`arXiv:1510.03865`] [INSPIRE].